Unfitted hybrid high-order methods for the wave equation

Erik Burman, Omar Duran, Alexandre Ern

Unfitted hybrid high-order methods for the wave equation

Erik Burman* Omar Duran† Alexandre Ern‡

December 22, 2020

Abstract

We design an unfitted hybrid high-order (HHO) method for the wave equation. The wave propagates in a domain where a curved interface separates subdomains with different material properties. The key feature of the discretization method is that the interface can cut more or less arbitrarily through the mesh cells. We address both the second-order formulation in time of the wave equation and its reformulation as a first-order system. We prove H^1-error estimates for a space semi-discretization in space of the second-order formulation, leading to optimal convergence rates for smooth solutions. Numerical experiments illustrate the theoretical findings and show that the proposed numerical schemes can be used to simulate accurately the propagation of acoustic waves in heterogeneous media, with meshes that are not fitted to the geometry. For the second-order formulation, the implicit, second-order accurate Newmark scheme is used for the time discretization, whereas (diagonally-implicit or explicit) Runge–Kutta schemes up to fourth-order accuracy are used for the first-order formulation. In the explicit case, we study the CFL condition on the time step and observe that the unfitted approach combined with local cell agglomeration leads to a comparable condition as when using fitted meshes.

Mathematics Subjects Classification. 65M12, 65M60, 74J10, 74S05.
Keywords. Hybrid high-order methods, unfitted mesh, error analysis, wave equation, heterogeneous media

1 Introduction

The accurate numerical approximation of wave phenomena is important in many applications. In particular, in medical imagining problems such as photo acoustic tomography, or geophysical applications involving seismic waves, it is paramount to be able to accurately approximate wave propagation through domains with complex geometry that are heterogeneous, that is, consisting of several subdomains with different physical characteristics. Either solid layers with varying wave speed can be considered, or the coupling between fluid and solid domains, where the model changes from the equations of acoustics to the equations of elastodynamics. It is also important to be able to handle problems where the ratio between the characteristic length scale of the domain and the wave length is large, which is typically the case for high frequency problems in medical applications or the propagation of seismic waves over large distances. Moreover, the

*Department of Mathematics, University College London, London, UK–WC1E 6BT, UK. E-mail address: e.burman@ucl.ac.uk
†CERMICS, Ecole des Ponts, 77455 Marne la Vallée cedex 2, and INRIA Paris, 75589 Paris, France. E-mail address: omar.duran@enpc.fr
‡CERMICS, Ecole des Ponts, 77455 Marne la Vallée cedex 2, and INRIA Paris, 75589 Paris, France. E-mail address: alexandre.ern@enpc.fr

geometry can be given by measurements, have curved boundaries or even be an unknown of the problem. These design constraints indicate the need for a method that handle heterogeneous material parameters (or models), propagates waves with low dissipation and dispersion, and is flexible for the integration of complex geometries.

To obtain a method that meets the above requirements, we herein combine the unfitted hybrid high order (HHO) method introduced in [10] for elliptic interface problems and further developed in [6] with the HHO methods for wave equations recently proposed and studied numerically in [8] and analyzed in the space semi-discrete case in [9]. The high order approximation of the method allows for good accuracy and low dispersion, while the unfitted character allows for great flexibility in the integration of interface geometries. In the context of stationary elliptic interface problems, the method can handle heterogeneous physical parameters and is robust for high-contrast problems. In this work, we handle the heterogeneous setting but do not explore the robustness with respect to high contrast. Finally, static condensation allows for an efficient numerical solution of the system resulting from the high-order discretization, by the local elimination of all the unknowns attached to the mesh cells.

HHO methods were introduced in [18] for linear diffusion problems and in [17] for locking-free linear elasticity. These methods rely on a pair of unknowns, combining polynomials attached to the mesh faces and to the mesh cells, and the cell unknowns can be eliminated locally by a static condensation procedure. HHO methods were bridged to hybridizable discontinuous Galerkin (HDG) methods and to nonconforming virtual element methods (ncVEM) in [13]. HHO methods also share similar devising principles with weak Galerkin (WG) methods [36]. In the unfitted HHO method, interfaces or boundaries are allowed to cut through the cells in a very general fashion. The interface conditions are then integrated on the cell-level and eliminated in the static condensation procedure. To avoid instabilities arising due to interface cell intersections resulting in very small or anisotropic sub-cells, a local cell-agglomeration algorithm has been designed in [6], drawing on earlier ideas from [24, 10]. Notice that the cell-agglomeration procedure crucially exploits the polyhedral features of HHO methods.

In the case of fitted meshes, HHO methods applied to the wave equation were devised and investigated numerically in [8], where in particular the significant improvement of solution quality for heterogeneous problems obtained by high-order approximation was showcased. The methods were analyzed in [9], leading to H^1-error estimates decaying with rate $\mathcal{O}(h^{k+1})$ for smooth solutions and L^2-error estimates decaying with rate $\mathcal{O}(h^{k+2})$ (assuming full elliptic regularity pickup). Here, k denotes the polynomial order of the skeletal unknowns. Numerical investigations of the method applied to the elastic wave equations were also reported. In the present paper, we focus on the propagation of acoustic waves in heterogeneous media using unfitted meshes. Considering both the second-order scalar wave equation and its first-order system formulation, we design unfitted HHO methods. In the case of the second-order form with space semi-discretization, we propose an error analysis in the H^1-norm, drawing on the ideas of [9] for the fitted HHO method applied to the wave equation. The analysis shows that the unfitted HHO method has similar accuracy as the fitted version discussed above. In the numerical section, we show, by comparing with the fitted method, that the perturbation introduced by the unfitted geometries is moderate.

Many numerical methods exist for the semi-discretization in space of the wave equation. High-order continuous finite elements (cG) are reviewed, e.g., in [16]. Discontinuous Galerkin (dG) methods have been successfully applied to the wave equation, written either as a first-order system [21, 27] or in its original second-order formulation in time [23]. Hybridizable dG (HDG) methods have been devised in [28, 31] for the first-order formulation, whereas the second-order formulation in time has been considered in [29, 14] with an eye toward conservation properties. The convergence analysis of HDG schemes has been performed in [15] in the time-continuous case

and in [22] by considering a Petrov–Galerkin time discretization. The design of HDG methods for geophysical applications and with special focus on the coupling of acoustics and elastodynamics was considered in [35]. Unfitted methods for wave equations were first introduced in [32] using cG and the cutFEM framework [7], with ghost penalty stabilization [5] to ensure the robustness with respect to the interface position. The extension to high-order cG-methods was considered in [33] and an extension to elastodynamics in [34]. A cut finite element methods using cG and lumped mass explicit time stepping was proposed in [11] using discrete extension operators, that generalizes the cG agglomeration procedure of [2]. The use of hybridized nonconforming unfitted methods is much less explored. Recently, a numerical study of the use of local time-stepping as an alternative to cell agglomeration in the context of cut hybrid discontinuous Galerkin methods (placing degrees of freedom on the curved boundary) was proposed in [30].

This paper is organized as follows. In Section 2, we present the model problem. In Section 3, we introduce the unfitted HHO method and the tools from [10, 6] that are used for its formulation and analysis. The application of the framework to the wave equation is considered in Section 4 for the second-order formulation in time and in Section 5 for the first-order formulation. In Section 6, we perform the error analysis, focusing for brevity on the second-order formulation. In Section 7, we discuss numerical results to verify the convergence rates predicted by the theory. We also study the integration for curved interfaces to ensure that the results are not polluted by under-resolved geometry. Then we consider different methods for the time discretization: the implicit, second-order accurate Newmark scheme for the second-order formulation and Runge–Kutta (RK) schemes up to accuracy order four (diagonally-implicit or explicit) for the first-order formulation. We compare the performances of the fitted and the unfitted methods on a model problem with a flat interface for which a semi-analytical solution is available at least over a certain time window. We then consider a curved interface and compare the results of the unfitted method using various time integration schemes, including a study of the CFL condition for the explicit RK schemes. Finally, we draw some conclusions in Section 8.

2 Model problem

Let Ω be a polyhedral domain in $\mathbb{R}^d$, $d \in \{2,3\}$ (open, bounded, connected, Lipschitz subset of $\mathbb{R}^d$) with boundary $\partial\Omega$. Let $J := (0, T_\mathrm{f})$ be the time interval with $T_\mathrm{f} > 0$. We use standard notation for the Lebesgue, Sobolev, and Bochner–Sobolev spaces. Boldface notation is used for vectors and vector-valued fields. For a subset $S \subset \mathbb{R}^d$, we denote $(\cdot,\cdot)_S$ the $L^2(S)$-inner product with appropriate Lebesgue measure and $\|\cdot\|_S$ the induced norm. For a weight function $\phi \in L^\infty(\Omega)$ taking positive values uniformly bounded from below away from zero, we use the shorthand notation $\|\cdot\|_{\phi;S} := \|\phi^{\frac{1}{2}}\cdot\|_S$, together with a similar notation for vector-valued fields.

Consider a partition of Ω into two disjoint subdomains $\overline{\Omega} = \overline{\Omega_1} \cup \overline{\Omega_2}$ with the interface $\Gamma := \partial\Omega_1 \cap \partial\Omega_2$. The interface Γ is assumed to be a smooth $(d-1)$-dimensional manifold of class C^2 that is not self-intersecting. Our goal is to approximate the solution $p : J \times (\Omega_1 \cup \Omega_2) \to \mathbb{R}$ of the following acoustic wave propagation problem with interface:

$$\frac{1}{\kappa}\partial_{tt} p - \nabla\cdot\left(\frac{1}{\rho}\nabla p\right) = f \qquad \text{in } J\times(\Omega_1\cup\Omega_2), \tag{1a}$$

$$[\![p]\!]_\Gamma = 0, \quad [\![\tfrac{1}{\rho}\nabla p]\!]_\Gamma\cdot\boldsymbol{n}_\Gamma = 0 \qquad \text{on } J\times\Gamma, \tag{1b}$$

$$p(0) = p_0, \quad \partial_t p(0) = v_0, \qquad \text{in } \Omega, \tag{1c}$$

$$p = 0, \qquad \text{on } J\times\partial\Omega, \tag{1d}$$

where the homogeneous Dirichlet boundary condition (1d) is considered for simplicity. The data

are $f \in L^2(J;L^2(\Omega))$, $p_0 \in H_0^1(\Omega)$, and $v_0 \in H_0^1(\Omega)$. For simplicity, we assume that the material parameters κ and ρ are constant in each subdomain Ω_i, $i \in \{1,2\}$, and we set $\kappa_i := \kappa_{|\Omega_i}$ and $\rho_i := \rho_{|\Omega_i}$. Recall that $c_i := \left(\frac{\kappa_i}{\rho_i}\right)^{\frac{1}{2}}$ is the wave speed in each subdomain Ω_i. The unit normal vector $\boldsymbol{n}_\Gamma$ to Γ conventionally points from Ω_1 to Ω_2 where the numbering of the subdomains corresponds to $\rho_1 \geq \rho_2$. For a smooth enough function v defined on $\Omega_1 \cup \Omega_2$, we denote its jump across Γ as $[\![v]\!]_\Gamma := v_{|\Omega_1} - v_{|\Omega_2}$. Notice that we could also consider the more general jump conditions $[\![p]\!]_\Gamma = g_D \in L^2(J;H^{\frac{1}{2}}(\Gamma))$ and $[\![\frac{1}{\rho}\nabla p]\!]_\Gamma \cdot \boldsymbol{n}_\Gamma = g_N \in L^2(J;L^2(\Gamma))$.

3 Setting for unfitted HHO methods

In this section, we introduce the notation for unfitted meshes and define the key ingredients for the unfitted HHO method.

3.1 Unfitted meshes

Let $(\mathcal{T}_h)_{h>0}$ be a sequence of meshes of Ω. The meshes can have cells that are polyhedra in $\mathbb{R}^d$ with planar faces, and hanging nodes are also possible. The mesh cells are taken to be open sets in $\mathbb{R}^d$. For all $T \in \mathcal{T}_h$, h_T denotes the diameter of the cell T and $\boldsymbol{n}_T$ the unit normal on ∂T pointing outward T. We set conventionally $h := \max_{T\in\mathcal{T}_h} h_T$. The mesh sequence is assumed to be shape-regular, i.e., for all $h > 0$, $\mathcal{T}_h$ admits a matching simplicial sub-mesh $\mathcal{T}_h'$ such that any cell (or face) of $\mathcal{T}_h'$ is a subset of a cell (or face) of $\mathcal{T}_h$, and there exists a mesh-regularity parameter $\rho > 0$ such that for all $h > 0$, all $T \in \mathcal{T}_h$, and all $S \in \mathcal{T}_h'$ such that $S \subset T$, we have $\rho h_S \leq r_S$ and $\rho h_T \leq h_S$, where r_S denotes the inradius of the simplex S. The mesh faces are collected in the set $\mathcal{F}_h$.

Let us define the partition $\mathcal{T}_h = \mathcal{T}_h^1 \cup \mathcal{T}_h^\Gamma \cup \mathcal{T}_h^2$, where the subsets

$$\mathcal{T}_h^i := \{T \in \mathcal{T}_h \mid T \subset \Omega_i\} \qquad \forall i \in \{1,2\}, \tag{2a}$$

$$\mathcal{T}_h^\Gamma := \{T \in \mathcal{T}_h \mid T \cap \Gamma \neq \emptyset\}, \tag{2b}$$

collect respectively the mesh cells inside the subdomain Ω_i, $i \in \{1,2\}$ (the uncut cells), and those cut by the interface Γ (the cut cells). For every cut cell $T \in \mathcal{T}_h^\Gamma$ and all $i \in \{1,2\}$, we define

$$T^i := T \cap \Omega_i, \qquad T^\Gamma := T \cap \Gamma. \tag{3}$$

For all $i \in \{1,2\}$, the boundary $\partial(T^i)$ of the sub-cell T^i is decomposed as

$$\partial(T^i) := (\partial T)^i \cup T^\Gamma, \qquad (\partial T)^i := \partial T \cap (\Omega_i \cup \partial\Omega). \tag{4}$$

To unify the notation, for every uncut cell $T \in \mathcal{T}_h^i$, $i \in \{1,2\}$, we set

$$T^i := T, \quad T^{\bar{\imath}} := \emptyset, \quad (\partial T)^i := \partial T, \quad (\partial T)^{\bar{\imath}} := \emptyset, \quad T^\Gamma := \emptyset, \tag{5}$$

where $\bar{\imath} := 3 - i$ (so that $\bar{1} = 2$ and $\bar{2} = 1$).

Three assumptions on the mesh are needed. The first one quantifies how well the interface cuts the mesh cells, the second one quantifies how well the mesh resolves the interface and the third one requires the mesh not to be excessively graded. In the sequel $B(\boldsymbol{x}, r)$ denotes the ball of center $\boldsymbol{x}$ and radius r.

Assumption 3.1 (Cut cells)**.** *There is $\delta \in (0,1)$ such that, for all $T \in \mathcal{T}_h^\Gamma$ and all $i \in \{1,2\}$, there is $\tilde{\boldsymbol{x}}_{T^i} \in T^i$ such that $B(\tilde{\boldsymbol{x}}_{T^i}, \delta h_T) \subset T^i$.*

Assumption 3.2 (Resolving Γ). *There is $\gamma \in (0,1)$ such that, for all $T \in \mathcal{T}_h^\Gamma$, there is a point $\check{\boldsymbol{x}}_T \in \mathbb{R}^d$ such that setting $T^\dagger := B(\check{\boldsymbol{x}}_T, \gamma^{-1} h_T)$ we have the following properties:* (i) *$T \subset T^\dagger$;* (ii) *for all $\boldsymbol{s} \in T^\Gamma$, $d(\check{\boldsymbol{x}}_T, T_{\boldsymbol{s}}\Gamma) \geq \gamma h_T$, where $T_{\boldsymbol{s}}\Gamma$ is the tangent plane to Γ at the point $\boldsymbol{s}$;* (iii) *For all $F \in \mathcal{F}_{\partial T}$, there is $\boldsymbol{x}_F \in T^\dagger$ such that $d(\boldsymbol{x}_F, F) \geq \gamma h_T$.*

Assumption 3.3 (Mild mesh grading). *For all $T \in \mathcal{T}_h$, let the neighboring layers $\Delta_j(T) \subset \mathbb{R}^d$ be defined by induction as $\Delta_0(T) := T$ and $\Delta_{j+1}(T) := \{T' \in \mathcal{T}_h \mid \overline{T'} \cap \overline{\Delta_j(T)} \neq \emptyset\}$ for all $j \in \mathbb{N}$. There is $n_0 \in \mathbb{N}$ such that for all $T \in \mathcal{T}_h$, the ball $T^\dagger$ introduced in Assumption 3.2 satisfies $T^\dagger \subset \Delta_{n_0}(T)$.*

It is shown in [10, 6] that if the mesh is fine enough, it is possible to devise a cell agglomeration procedure so that, choosing the parameter δ small enough (depending on the regularity parameter ρ), Assumption 3.1 is fulfilled. It is shown in [10, Lemma 6.1] that if the mesh is fine enough with respect to the curvature of the interface, the points (i) and (ii) of Assumption 3.2 hold true. Moreover the point (iii) of this assumption can be established by invoking the shape-regularity of the mesh as shown in the proof of [10, Lemma 3.3]. The role of Assumption 3.1 in the analysis is to provide discrete (inverse) inequalities in the cut cells (see to [10, Lemma 3.4] and [6, Lemma 3.4] for proofs). The role of Assumption 3.2 is to provide a multiplicative trace inequality that is needed to establish optimal approximation properties on the faces and on the interface within the cut cells (see [10, Lemma 3.3] for the proof).

Lemma 3.4 (Discrete inverse inequalities). *Let Assumption 3.1 be fulfilled. Let $\ell \in \mathbb{N}$. There is c_{disc}, depending on ρ, δ, and ℓ, such that, for all $T \in \mathcal{T}_h$, all $i \in \{1,2\}$ and all $v_{T^i} \in \mathbb{P}^\ell(T^i)$, the following inequalities hold true:*

- *(Discrete trace inequality) $\|v_{T^i}\|_{\partial(T^i)} \leq c_{\mathrm{disc}} h_T^{-\frac{1}{2}} \|v_{T^i}\|_{T^i}$.*
- *(Discrete inverse inequality) $\|\nabla v_{T^i}\|_{T^i} \leq c_{\mathrm{disc}} h_T^{-1} \|v_{T^i}\|_{T^i}$.*
- *(Discrete Poincaré inequality) Assuming that $(v_{T^i}, 1)_{B(\tilde{\boldsymbol{x}}_{T^i}, h_T)} = 0$, we have $\|v_{T^i}\|_{T^i} \leq c_{\mathrm{disc}} h_T \|\nabla v_{T^i}\|_{T^i}$.*

Lemma 3.5 (Multiplicative trace inequality). *Let Assumption 3.2 be fulfilled. There is $c_{\mathrm{mtr}} > 0$, depending on ρ and γ, such that for all $T \in \mathcal{T}_h$, all $v \in H^1(T^\dagger)$, and all $i \in \{1,2\}$,*

$$\|v\|_{\partial(T^i)} \leq c_{\mathrm{mtr}} \left(h_T^{-\frac{1}{2}} \|v\|_{T^\dagger} + \|v\|_{T^\dagger}^{\frac{1}{2}} \|\nabla v\|_{T^\dagger}^{\frac{1}{2}} \right). \tag{6}$$

In what follows, we use the convention $A \lesssim B$ to abbreviate the inequality $A \leq CB$ for positive real numbers A and B, where the constant C only depends on the polynomial degree $k \geq 0$, the mesh parameters ρ, δ, γ and n_0, and the above constants c_{disc} and c_{mtr}.

3.2 Discrete unknowns for unfitted HHO methods

For a subset $S \subset \mathbb{R}^d$ consisting of one mesh (sub)cell or one mesh (sub)face, we denote $\mathbb{P}^\ell(S)$ (resp. $\mathbb{P}^\ell(S;\mathbb{R}^d)$) the space composed of the restriction to S of scalar-valued (resp. vector-valued) polynomials of total degree at most $\ell \geq 0$. Whenever $S = \emptyset$, we abuse the notation by writing $\mathbb{P}^\ell(S) := \{0\}$ and $(\cdot,\cdot)_{L^2(S)} := 0$.

Let $k \geq 0$ be the polynomial degree used in the unfitted HHO method. For every uncut cell $T \in \mathcal{T}_h^i$, $i \in \{1,2\}$, the local discrete HHO unknowns are a pair of functions: one polynomial of degree at most $(k+1)$ attached to the cell T and one polynomial of degree at most k attached

to each face $F \in \mathcal{F}_{\partial T}$, where $\mathcal{F}_{\partial T}$ comprises all the faces composing the boundary ∂T of the cell T. We use the notation

$$\hat{v}_T := (v_T, v_{\partial T}) \in \mathbb{P}^{k+1}(T) \times \mathbb{P}^k(\mathcal{F}_{\partial T}), \tag{7}$$

with $\mathbb{P}^k(\mathcal{F}_{\partial T}) := \bigtimes_{F \in \mathcal{F}_{\partial T}} \mathbb{P}^k(F)$. For every cut cell $T \in \mathcal{T}_h^\Gamma$, we double the HHO unknowns, so as to have the usual HHO unknowns available on each sub-cell, up to the interface Γ where there are no unknowns. Thus, the local HHO unknowns in every cut cell $T \in \mathcal{T}_h^\Gamma$ are

$$\hat{v}_T := (v_{T^1}, v_{T^2}, v_{(\partial T)^1}, v_{(\partial T)^2}) \in \hat{V}_T := \mathbb{P}^{k+1}(T^1) \times \mathbb{P}^{k+1}(T^2) \times \mathbb{P}^k(\mathcal{F}_{(\partial T)^1}) \times \mathbb{P}^k(\mathcal{F}_{(\partial T)^2}), \tag{8}$$

where $\mathcal{F}_{(\partial T)^i} := \{F^i := F \cap \Omega_i \mid F \in \mathcal{F}_{\partial T}\}$ is the collection of the (sub)faces composing $(\partial T)^i$ and $\mathbb{P}^k(\mathcal{F}_{(\partial T)^i}) := \bigtimes_{F^i \in \mathcal{F}_{(\partial T)^i}} \mathbb{P}^k(F^i)$, $i \in \{1,2\}$. It is also convenient to regroup the local unknowns on each side of the interface by means of the notation $\hat{v}_{T^i} := (v_{T^i}, v_{(\partial T)^i}) \in \mathbb{P}^{k+1}(T^i) \times \mathbb{P}^k(\mathcal{F}_{(\partial T)^i})$, $i \in \{1,2\}$. The HHO unknowns are shown in Fig. 1, where the number of bullets represents the number of degrees of freedom attached to each geometric entity. The left panel of Fig. 1 shows three uncut cells, the central panel shows three cut cells, and the right panel shows the result of local agglomeration for the three cut cells. To unify the notation between cut and uncut cells, we define $\hat{V}_T$ as in (8) for every uncut cell $T \in \mathcal{T}_h^i$, $i \in \{1,2\}$. With this abuse of notation, we have $\hat{v}_T := (v_T, 0, v_{\partial T}, 0)$ for all $T \in \mathcal{T}_h^1$ and $\hat{v}_T := (0, v_T, 0, v_{\partial T})$ for all $T \in \mathcal{T}_h^2$.

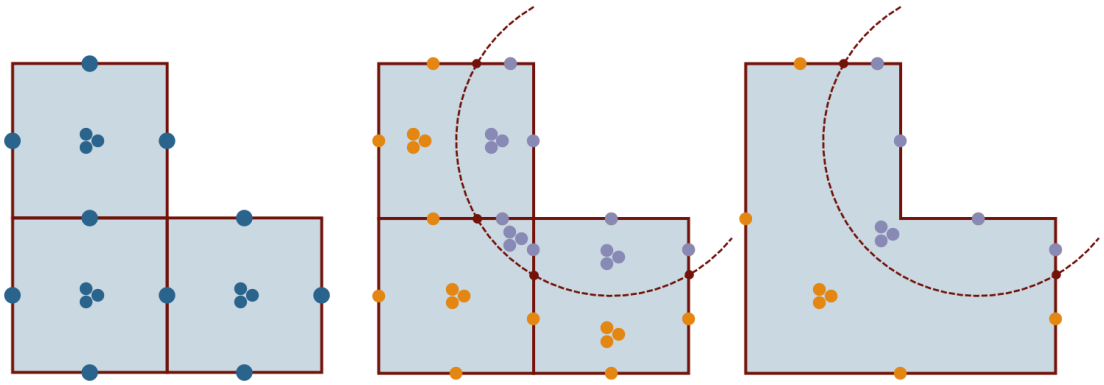

Figure 1: Local HHO unknowns for $k = 0$. Left: three uncut cells; center: three cut cells; right: the three cut cells after local agglomeration into one polyhedral cell. Each bullet represents one basis function, and the red dashed line represents the interface Γ.

3.3 Local gradient reconstruction

As usual in HHO methods, a key ingredient is a local gradient reconstruction operator. In every cut cell $T \in \mathcal{T}_h^\Gamma$, there are two gradient reconstruction operators $\boldsymbol{G}_{T^i}^k : \hat{V}_T \to \mathbb{P}^k(T^i; \mathbb{R}^d)$, $i \in \{1,2\}$ (an alternative choice is to reconstruct the gradient in $\nabla \mathbb{P}^{k+1}(T^i)$ in the spirit of the original HHO method [18, 17]; the present choice is more suitable in view of extensions to nonlinear problems). For every cut cell $T \in \mathcal{T}_h^\Gamma$ and every $\hat{v}_T \in \hat{V}_T$, letting $[\![v_T]\!]_\Gamma := v_{T^1} - v_{T^2}$, we set

$$(\boldsymbol{G}_{T^1}^k(\hat{v}_T), \boldsymbol{q})_{T^1} := (\nabla v_{T^1}, \boldsymbol{q})_{T^1} + (v_{(\partial T)^1} - v_{T^1}, \boldsymbol{q}\cdot\boldsymbol{n}_T)_{(\partial T)^1} - ([\![v_T]\!]_\Gamma, \boldsymbol{q}\cdot\boldsymbol{n}_\Gamma)_{T^\Gamma}, \tag{9}$$

$$(\boldsymbol{G}_{T^2}^k(\hat{v}_T), \boldsymbol{q})_{T^2} := (\nabla v_{T^2}, \boldsymbol{q})_{T^2} + (v_{(\partial T)^2} - v_{T^2}, \boldsymbol{q}\cdot\boldsymbol{n}_T)_{(\partial T)^2}, \tag{10}$$

for all $\boldsymbol{q} \in \mathbb{P}^k(T^1;\mathbb{R}^d)$ in (9) and all $\boldsymbol{q} \in \mathbb{P}^k(T^2;\mathbb{R}^d)$ in (10). Notice that $\boldsymbol{G}^k_{T^2}(\hat{v}_T)$ only depends on $\hat{v}_{T^2}$, whereas $\boldsymbol{G}^k_{T^1}(\hat{v}_T)$ depends on both $\hat{v}_{T^1}$ and $\hat{v}_{T^2}$ owing to the jump term on the right-hand side of (9). The difference in the reconstruction between the two subdomains is not essential here since we do not explore the strongly-contrasted case, and one can also consider the reconstruction variant discussed in [6, Sec. 2.5]. Using the above conventions on the notation, we use the same definitions for every uncut cell $T \in \mathcal{T}_h^i$, $i \in \{1,2\}$, leading to $(\boldsymbol{G}^k_{T^i}(\hat{v}_T), \boldsymbol{q})_{T^i} := (\nabla v_{T^i}, \boldsymbol{q})_{T^i} + (v_{(\partial T)^i} - v_{T^i}, \boldsymbol{q}\cdot\boldsymbol{n}_T)_{(\partial T)^i}$ for all $\boldsymbol{q} \in \mathbb{P}^k(T^i;\mathbb{R}^d)$, and $\boldsymbol{G}^k_{T^i}(\hat{v}_T) := \boldsymbol{0}$. Recalling that $T^i := T$ and $(\partial T)^i := \partial T$, $\boldsymbol{G}^k_{T^i}(\hat{v}_T)$ corresponds to one of the possible HHO gradient reconstructions in the fitted case (see, e.g., [4, 1]).

4 Wave equation: second-order formulation

In this section, we show how to apply the unfitted HHO method to the second-order formulation in time of the acoustic wave equation. Let us set for all $i \in \{1,2\}$,

$$V_{\mathcal{T}^i} := \bigtimes_{T\in\mathcal{T}_h} \mathbb{P}^{k+1}(T^i), \qquad V_{\mathcal{F}^i} := \bigtimes_{F\in\mathcal{F}_h} \mathbb{P}^k(F^i). \tag{11}$$

We define the global discrete spaces

$$\hat{V}_h := V_{\mathcal{T}} \times V_{\mathcal{F}}, \qquad V_{\mathcal{T}} := V_{\mathcal{T}^1} \times V_{\mathcal{T}^2}, \qquad V_{\mathcal{F}} := V_{\mathcal{F}^1} \times V_{\mathcal{F}^2}. \tag{12}$$

For all $\hat{v}_h \in \hat{V}_h$, we write $\hat{v}_h = (v_{\mathcal{T}}, v_{\mathcal{F}})$ with $v_{\mathcal{T}} = (v_{\mathcal{T}^1}, v_{\mathcal{T}^2}) \in V_{\mathcal{T}}$ and $v_{\mathcal{F}} = (v_{\mathcal{F}^1}, v_{\mathcal{F}^2}) \in V_{\mathcal{F}}$. Moreover, for all T in $\mathcal{T}_h$, we denote $\hat{v}_T := (v_{T^1}, v_{T^2}, v_{(\partial T)^1}, v_{(\partial T)^2})$ the local components of $\hat{v}_h$ respectively attached to T^1, T^2, $(\partial T)^1$, and $(\partial T)^2$. We denote $\hat{V}_{h0}$ the subspace of $\hat{V}_h$ where all degrees of freedom attached to the faces composing $\partial\Omega$ are null.

The global discrete bilinear form is assembled cellwise by summing the contributions of local discrete bilinear forms. For all $T \in \mathcal{T}_h$ and all $\hat{v}_T, \hat{w}_T \in \hat{V}_T$, we set

$$b_T(\hat{v}_T, \hat{w}_T) := \sum_{i\in\{1,2\}} \Big\{ (\boldsymbol{G}^k_{T^i}(\hat{v}_T), \boldsymbol{G}^k_{T^i}(\hat{w}_T))_{\rho_i^{-1};T^i} + s_{T^i}(\hat{v}_{T^i}, \hat{w}_{T^i}) \Big\} + s_T^\Gamma(\hat{v}_T, \hat{w}_T), \tag{13}$$

with

$$s_{T^i}(\hat{v}_{T^i}, \hat{w}_{T^i}) := (\rho_i h_T)^{-1} \Big(\Pi^k_{(\partial T)^i}(v_{T^i} - v_{(\partial T)^i}), w_{T^i} - w_{(\partial T)^i} \Big)_{(\partial T)^i}, \tag{14}$$

$$s_T^\Gamma(\hat{v}_T, \hat{w}_T) := (\rho_1 h_T)^{-1} (\llbracket v_T \rrbracket_\Gamma, \llbracket w_T \rrbracket_\Gamma)_{T^\Gamma}, \tag{15}$$

where $\Pi^k_{(\partial T)^i}$ denotes the L^2-orthogonal projector onto $\mathbb{P}^k(\mathcal{F}_{(\partial T)^i})$. Notice that the role of s_{T^i} is to weakly enforce the matching between cell- and face-based HHO unknowns in all the faces inside the subdomains, whereas the role of s_T^Γ is to weakly enforce the first jump condition in (1b). We then define the global bilinear form $b_h : \hat{V}_h \times \hat{V}_h \to \mathbb{R}$ such that

$$b_h(\hat{v}_h, \hat{w}_h) := \sum_{T\in\mathcal{T}_h} b_T(\hat{v}_T, \hat{w}_T) = (\boldsymbol{G}^k_{\mathcal{T}}(\hat{v}_h), \boldsymbol{G}^k_{\mathcal{T}}(\hat{w}_h))_{\rho^{-1};\Omega} + s_h(\hat{v}_h, \hat{w}_h) + s_h^\Gamma(\hat{v}_h, \hat{w}_h), \tag{16}$$

with the global reconstruction operator such that $\boldsymbol{G}^k_{\mathcal{T}}(\hat{v}_h)_{|T^i} := \boldsymbol{G}_{T^i}(\hat{v}_T)$ for all $T \in \mathcal{T}_h$, all $i \in \{1,2\}$, and all $\hat{v}_h \in \hat{V}_h$, and the global stabilization bilinear forms such that $s_h(\hat{v}_h, \hat{w}_h) := \sum_{T\in\mathcal{T}_h} \sum_{i\in\{1,2\}} s_{T^i}(\hat{v}_{T^i}, \hat{w}_{T^i})$ and $s_h^\Gamma(\hat{v}_h, \hat{w}_h) := \sum_{T\in\mathcal{T}_h} s_T^\Gamma(\hat{v}_T, \hat{w}_T)$.

The space semi-discrete HHO scheme for the second-order wave equation consists of finding $\hat{p}_h := (p_{\mathcal{T}}, p_{\mathcal{F}}) \in C^2(\overline{J}; \hat{V}_{h0})$ such that for all $t \in \overline{J}$,

$$(\partial_{tt} p_{\mathcal{T}}(t), q_{\mathcal{T}})_{\frac{1}{\kappa};\Omega} + b_h(\hat{p}_h(t), \hat{q}_h) = (f(t), q_{\mathcal{T}})_\Omega, \tag{17}$$

for all $\hat{q}_h := (q_{\mathcal{T}}, q_{\mathcal{F}}) \in \hat{V}_{h0}$. The initial conditions for (17) only concern $p_{\mathcal{T}}$ and are as follows:

$$p_{\mathcal{T}}(0)_{|\Omega_i} = \Pi_{\mathcal{T}^i}^{k+1}(p_{0|\Omega_i}), \qquad \partial_t p_{\mathcal{T}}(0)_{|\Omega_i} = \Pi_{\mathcal{T}^i}^{k+1}(v_{0|\Omega_i}), \qquad i \in \{1,2\}, \tag{18}$$

where $\Pi_{\mathcal{T}^i}^{k+1}$ is the L^2-orthogonal projection onto $V_{\mathcal{T}^i}$, $i \in \{1,2\}$. The boundary condition is encoded in the fact that $\hat{p}_h(t) \in \hat{V}_{h0}$ for all $t \in \overline{J}$. Notice that since the space semi-discrete solution is smooth in time, (17) holds at the initial time which implies that $p_{\mathcal{F}}(0) \in V_{\mathcal{F}}$ is uniquely determined by the equations $b_h((p_{\mathcal{T}}(0), p_{\mathcal{F}}(0)), (0, q_{\mathcal{F}})) = 0$ for all $q_{\mathcal{F}} \in V_{\mathcal{F}}$ with $p_{\mathcal{T}}(0)$ specified in (18) and the boundary condition enforcing to zero the components of $p_{\mathcal{F}}(0)$ attached to the boundary faces.

Let $N_{\mathcal{T}} := \dim(V_{\mathcal{T}})$ and $N_{\mathcal{F}} := \dim(V_{\mathcal{F}})$. Let $(\mathsf{P}_{\mathcal{T}}(t), \mathsf{P}_{\mathcal{F}}(t)) \in \mathbb{R}^{N_{\mathcal{T}} \times N_{\mathcal{F}}}$ be the (time-dependent) component vectors of the space semi-discrete solution $\hat{p}_h(t) := (p_{\mathcal{T}}(t), p_{\mathcal{F}}(t)) \in \hat{V}_{h0}$ once bases $\{\varphi_i\}_{1 \le i \le N_{\mathcal{T}}}$ and $\{\psi_j\}_{1 \le j \le N_{\mathcal{F}}}$ for $V_{\mathcal{T}}$ and $V_{\mathcal{F}}$, respectively, have been chosen. Let $\mathsf{F}_{\mathcal{T}}(t) \in \mathbb{R}^{N_{\mathcal{T}}}$ have components given by $\mathsf{F}_i(t) := (f(t), \varphi_i)_\Omega$ for all $t \in \overline{J}$ and all $1 \le i \le N_{\mathcal{T}}$. The algebraic realization of (18) is as follows: For all $t \in \overline{J}$,

$$\begin{bmatrix} \mathsf{M}_{\mathcal{T}\mathcal{T}} & 0 \\ 0 & 0 \end{bmatrix} \begin{bmatrix} \partial_{tt}\mathsf{P}_{\mathcal{T}}(t) \\ \bullet \end{bmatrix} + \begin{bmatrix} \mathsf{K}_{\mathcal{T}\mathcal{T}} & \mathsf{K}_{\mathcal{T}\mathcal{F}} \\ \mathsf{K}_{\mathcal{F}\mathcal{T}} & \mathsf{K}_{\mathcal{F}\mathcal{F}} \end{bmatrix} \begin{bmatrix} \mathsf{P}_{\mathcal{T}}(t) \\ \mathsf{P}_{\mathcal{F}}(t) \end{bmatrix} = \begin{bmatrix} \mathsf{F}_{\mathcal{T}}(t) \\ 0 \end{bmatrix}, \tag{19}$$

with the mass matrix $\mathsf{M}_{\mathcal{T}\mathcal{T}}$ associated with the inner product in $L^2(\frac{1}{\kappa};\Omega)$ and the cell basis functions, and the symmetric positive-definite stiffness matrix with blocks $\mathsf{K}_{\mathcal{T}\mathcal{T}}$, $\mathsf{K}_{\mathcal{T}\mathcal{F}}$, $\mathsf{K}_{\mathcal{F}\mathcal{T}}$, $\mathsf{K}_{\mathcal{F}\mathcal{F}}$ associated with the bilinear form b_h and the cell and face basis functions. The bullet stands for $\partial_{tt}\mathsf{P}_{\mathcal{F}}(t)$ which is irrelevant owing to the structure of the mass matrix. The matrices $\mathsf{M}_{\mathcal{T}\mathcal{T}}$ and $\mathsf{K}_{\mathcal{T}\mathcal{T}}$ are block-diagonal, but not the matrix $\mathsf{K}_{\mathcal{F}\mathcal{F}}$ since the components attached to faces belonging to the same cell are coupled together. Notice also that the sizes of the diagonal blocks $\mathsf{M}_{\mathcal{T}\mathcal{T}}$ and $\mathsf{K}_{\mathcal{T}\mathcal{T}}$ are different for the uncut and the cut cells.

Remark 4.1 (Fitted case)**.** *In the fitted case, the above HHO method has been devised in [8]. Moreover, using the ideas from [13] to bridge HHO and HDG methods, this method can be connected to the space semi-discrete HDG formulation from [14]. Notice that unfitted HHO methods use a mixed-order polynomial setting where the polynomials attached to the cells are one order higher than those attached to the faces. The stabilization bilinear form* (14) *on the faces inside each subdomain amounts to the Lehrenfeld–Schöberl HDG stabilization [25, 26].*

5 Wave equation: first-order formulation

In this section, we apply the unfitted HHO method to the first-order formulation in time of the acoustic wave equation. The first-order formulation is classically obtained by introducing two auxiliary variables, the scalar velocity $v := \partial_t p$ and the dual variable $\boldsymbol{\sigma} := \frac{1}{\rho}\nabla p$. This leads to the following coupled PDEs:

$$\begin{cases} \rho\partial_t \boldsymbol{\sigma} - \nabla v = \mathbf{0} \\ \dfrac{1}{\kappa}\partial_t v - \nabla\cdot\boldsymbol{\sigma} = f \end{cases} \qquad \text{in } J \times (\Omega_1 \cup \Omega_2), \tag{20}$$

together with the boundary condition $v = 0$ on $J \times \Gamma$ and the initial conditions $v(0) = v_0$ and $\boldsymbol{\sigma}(0) = \frac{1}{\rho}\nabla p_0$ in Ω. The jump conditions become $[\![v]\!]_\Gamma = 0$ and $[\![\boldsymbol{\sigma}]\!]_\Gamma \cdot \boldsymbol{n}_F = 0$ on Γ.

In the space semi-discrete case, one approximates v by a hybrid unknown $\hat{v}_h \in C^1(\overline{J}; \hat{V}_{h0})$ and $\boldsymbol{\sigma}$ by a cellwise unknown $\boldsymbol{\sigma}_\mathcal{T} \in C^1(\overline{J}; \boldsymbol{W}_\mathcal{T})$ where

$$\boldsymbol{W}_\mathcal{T} := \boldsymbol{W}_{\mathcal{T}^1} \times \boldsymbol{W}_{\mathcal{T}^2}, \qquad \boldsymbol{W}_{\mathcal{T}^i} := \bigtimes_{T \in \mathcal{T}_h} \mathbb{P}^k(T^i; \mathbb{R}^d). \tag{21}$$

The space semi-discrete problem reads as follows: For all $t \in \overline{J}$,

$$\begin{cases} (\partial_t \boldsymbol{\sigma}_\mathcal{T}(t), \boldsymbol{\tau}_\mathcal{T})_{\rho;\Omega} - (\boldsymbol{G}_\mathcal{T}(\hat{v}_h(t)), \boldsymbol{\tau}_\mathcal{T})_\Omega = 0, \\ (\partial_t v_\mathcal{T}(t), w_\mathcal{T})_{\frac{1}{\kappa};\Omega} + (\boldsymbol{\sigma}_\mathcal{T}(t), \boldsymbol{G}_\mathcal{T}(\hat{w}_h))_{\boldsymbol{L}^2(\Omega)} + \tilde{s}_h(\hat{v}_h(t), \hat{w}_h) + \tilde{s}_h^\Gamma(\hat{v}_h(t), \hat{w}_h) = (f(t), w_\mathcal{T})_\Omega, \end{cases} \tag{22}$$

for all $(\boldsymbol{\tau}_\mathcal{T}, \hat{w}_h) \in \boldsymbol{W}_\mathcal{T} \times \hat{V}_{h0}$, together with the initial conditions $\boldsymbol{\sigma}_\mathcal{T}(0) = \frac{1}{\rho}\boldsymbol{G}_\mathcal{T}(\Pi_\mathcal{T}^{k+1}(p_0), \Pi_\mathcal{F}^k(p_0))$ and $v(0) = \Pi_\mathcal{T}^{k+1}(v_0)$, where $\boldsymbol{G}_\mathcal{T}$ is defined in Section 4, $\Pi_\mathcal{T}^{k+1} := (\Pi_{\mathcal{T}^1}^{k+1}, \Pi_{\mathcal{T}^2}^{k+1})$, $\Pi_\mathcal{F}^k := (\Pi_{\mathcal{F}^1}^k, \Pi_{\mathcal{F}^2}^k)$, $\Pi_{\mathcal{T}^i}^{k+1}$ is the L^2-orthogonal projection onto $V_{\mathcal{T}^i}$, and $\Pi_{\mathcal{F}^i}^k$ that onto $V_{\mathcal{F}^i}$, $i \in \{1, 2\}$. Moreover, the stabilization bilinear forms are $\tilde{s}_h(\hat{v}_h, \hat{w}_h) := \sum_{T \in \mathcal{T}_h} \tilde{s}_T(\hat{v}_T, \hat{w}_T)$ and $\tilde{s}_h^\Gamma(\hat{v}_h, \hat{w}_h) := \sum_{T \in \mathcal{T}_h} \tilde{s}_T^\Gamma(\hat{v}_T, \hat{w}_T)$, with (compare with (14)-(15))

$$\tilde{s}_T(\hat{v}_T, \hat{w}_T) := \sum_{i \in \{1,2\}} \tilde{\tau}_{(\partial T)^i} \Big(\Pi_{(\partial T)^i}^k (v_{T^i} - v_{(\partial T)^i}), w_{T^i} - w_{(\partial T)^i} \Big)_{(\partial T)^i}, \tag{23}$$

$$\tilde{s}_T^\Gamma(\hat{v}_T, \hat{w}_T) := \tilde{\tau}_{T^\Gamma}([\![v_T]\!]_\Gamma, [\![w_T]\!]_\Gamma)_{T^\Gamma}. \tag{24}$$

We shall discuss two choices for the stabilization weights, either $\tilde{\tau}_{(\partial T)^i} := \frac{\ell_\Omega}{c_i}(\rho_i h_T)^{-1}$ and $\tilde{\tau}_{T^\Gamma} := \frac{\ell_\Omega}{c_1}(\rho_1 h_T)^{-1}$ (in short, we say $\tilde{\tau}_{\partial T} = \mathcal{O}(h^{-1})$) or $\tilde{\tau}_{(\partial T)^i} := (\rho_i c_i)^{-1}$ and $\tilde{\tau}_{T^\Gamma} := (\rho_1 c_1)^{-1}$ (in short, we say $\tilde{\tau}_{\partial T} = \mathcal{O}(1)$). Here, $\ell_\Omega := \mathrm{diam}(\Omega)$ is a global length scale introduced to remain dimensionally consistent.

Let $M_\mathcal{T} := \dim(\boldsymbol{W}_\mathcal{T}) = dN_\mathcal{T}^k$ and $\{\boldsymbol{\zeta}_i\}_{1 \le i \le M_\mathcal{T}}$ be the chosen basis for $\boldsymbol{W}_\mathcal{T}$. Let $\mathsf{Z}_\mathcal{T}(t) \in \mathbb{R}^{M_\mathcal{T}}$ and $(\mathsf{V}_\mathcal{T}(t), \mathsf{V}_\mathcal{F}(t)) \in \mathbb{R}^{N_\mathcal{T} \times N_\mathcal{F}}$ be the component vectors of $\boldsymbol{\sigma}_\mathcal{T}(t) \in \boldsymbol{W}_\mathcal{T}$ and $\hat{v}_h(t) \in \hat{V}_{h0}$, respectively. Let $\mathsf{M}_{\mathcal{T}\mathcal{T}}^{\boldsymbol{\sigma}}$ be the mass matrix associated with the inner product in $\boldsymbol{L}^2(\rho;\Omega)$ and the basis functions $\{\boldsymbol{\zeta}_i\}_{1 \le i \le M_\mathcal{T}}$, and recall that the mass matrix $\mathsf{M}_{\mathcal{T}\mathcal{T}}$ and the right-hand side vector $\mathsf{F}(t)$ are defined in Section 4. Let $\mathsf{S}_{\mathcal{T}\mathcal{T}}$, $\mathsf{S}_{\mathcal{T}\mathcal{F}}$, $\mathsf{S}_{\mathcal{F}\mathcal{T}}$, $\mathsf{S}_{\mathcal{F}\mathcal{F}}$ be the four blocks composing the matrix representing the stabilization bilinear form $\tilde{s}_h$. Let $\mathsf{G}_\mathcal{T} \in \mathbb{R}^{M_\mathcal{T} \times N_\mathcal{T}}$ and $\mathsf{G}_\mathcal{F} \in \mathbb{R}^{M_\mathcal{T} \times N_\mathcal{F}}$ be the (rectangular) matrices representing the gradient reconstruction operator. The algebraic realization of (22) is as follows: For all $t \in \overline{J}$,

$$\begin{bmatrix} \mathsf{M}_{\mathcal{T}\mathcal{T}}^{\boldsymbol{\sigma}} & 0 & 0 \\ 0 & \mathsf{M}_{\mathcal{T}\mathcal{T}} & 0 \\ 0 & 0 & 0 \end{bmatrix} \begin{bmatrix} \partial_t \mathsf{Z}_\mathcal{T}(t) \\ \partial_t \mathsf{V}_\mathcal{T}(t) \\ \bullet \end{bmatrix} + \begin{bmatrix} 0 & -\mathsf{G}_\mathcal{T} & -\mathsf{G}_\mathcal{F} \\ \mathsf{G}_\mathcal{T}^\dagger & \mathsf{S}_{\mathcal{T}\mathcal{T}} & \mathsf{S}_{\mathcal{T}\mathcal{F}} \\ \mathsf{G}_\mathcal{F}^\dagger & \mathsf{S}_{\mathcal{F}\mathcal{T}} & \mathsf{S}_{\mathcal{F}\mathcal{F}} \end{bmatrix} \begin{bmatrix} \mathsf{Z}_\mathcal{T}(t) \\ \mathsf{V}_\mathcal{T}(t) \\ \mathsf{V}_\mathcal{F}(t) \end{bmatrix} = \begin{bmatrix} 0 \\ \mathsf{F}_\mathcal{T}(t) \\ 0 \end{bmatrix}, \tag{25}$$

where the bullet stands for $\partial_t \mathsf{V}_\mathcal{F}(t)$ which is irrelevant owing to the structure of the mass matrix. Notice that the third equation in (25) implies that

$$\mathsf{S}_{\mathcal{F}\mathcal{F}} \mathsf{V}_\mathcal{F}(t) = -(\mathsf{G}_\mathcal{F}^\dagger \mathsf{Z}_\mathcal{T}(t) + \mathsf{S}_{\mathcal{F}\mathcal{T}} \mathsf{V}_\mathcal{T}(t)), \tag{26}$$

and that the sub-matrix $\mathsf{S}_{\mathcal{F}\mathcal{F}}$ is symmetric positive-definite. A crucial observation is that this sub-matrix is additionally block-diagonal, so that (26) is very cheap to invert.

Remark 5.1 (Fitted case)**.** *In the fitted case, the above HHO method has been devised in [8]. Owing to [13], this method can be bridged to the space semi-discrete HDG formulation from [28]. Notice though that [28] considers an equal-order setting for the cell and face unknowns and a stability weight $\tilde{\tau}_{\partial T} = \mathcal{O}(1)$.*

6 Error analysis for the second-order in time formulation

This section is devoted to the error analysis of the unfitted HHO method for the second-order formulation in time of the acoustic wave equation. The analysis combines ideas from [10, 6] concerning the stability and consistency of unfitted HHO methods with ideas from [9] concerning the analysis of fitted HHO methods for the wave equation. These latter ideas in turn draw on the error analysis from [20, 3] for continuous finite elements applied to the wave equation. We assume that the assumptions stated in Section 3.1 hold true.

6.1 Stability, approximation, and consistency

We equip the space $\hat{V}_{h0}$ with the norm

$$\|\hat{v}_h\|_{\hat{V}_{h0}}^2 := \sum_{T\in\mathcal{T}_h}\sum_{i\in\{1,2\}}\Big\{\|\nabla v_{T^i}\|_{\rho_i^{-1};T^i}^2 + (\rho_i h_T)^{-1}\|v_{(\partial T)^i} - v_{T^i}\|_{(\partial T)^i}^2\Big\} + (\rho_1 h_T)^{-1}\|[\![v_T]\!]_\Gamma\|_{T^\Gamma}^2. \tag{27}$$

We have the following important stability result [6, Lem. 3.6] (which only requires Assumption 3.1): There are $0 < \alpha \le \omega < +\infty$ such that

$$\alpha\|\hat{v}_h\|_{\hat{V}_{h0}}^2 \le b_h(\hat{v}_h,\hat{v}_h) \le \omega\|\hat{v}_h\|_{\hat{V}_{h0}}^2, \qquad \forall \hat{v}_h \in \hat{V}_{h0}. \tag{28}$$

The error analysis hinges on a suitable error decomposition defined by some approximation of the exact solution. To this purpose, following [6], we assume that there is a real number $\nu \in (\frac{1}{2}, k+1]$ such that the exact solution satisfies $p_{|\Omega_i} \in C^1(\overline{J};H^{1+\nu}(\Omega_i))$, $i\in\{1,2\}$, and we consider stable extension operators $E_i : H^{1+\nu}(\Omega_i) \to H^{1+\nu}(\mathbb{R}^d)$. For all $v \in H^1(\Omega_1\cup\Omega_2)$ with $v_i := v_{|\Omega_i}$ and all $T\in\mathcal{T}_h$, we then define

$$I_{T^i}^{k+1}(v_i) := (\Pi_{T^\dagger}^{k+1}(E_i(v_i)))_{|T^i} \in \mathbb{P}^{k+1}(T^i), \tag{29}$$

$$\hat{I}_T^k(v) := (I_{T^1}^{k+1}(v_1), I_{T^2}^{k+1}(v_2), \Pi_{(\partial T)^1}^k(v_1), \Pi_{(\partial T)^2}^k(v_2)) \in \hat{V}_T, \tag{30}$$

where $\Pi_{T^\dagger}^{k+1}$ denotes the L^2-orthogonal projector onto $\mathbb{P}^{k+1}(T^\dagger)$. Note that we do not project using the sub-cell T^i but the larger set $T^\dagger$ from Assumption 3.2 so as to invoke the optimal approximation properties of $I_{T^i}^{k+1}$ (see for instance [10, Lemma 5.6]). Indeed, if this assumption is fulfilled, we have for all $v\in L^2(\Omega)$ such that $v_i \in H^{1+\nu}(\Omega_i)$, $i\in\{1,2\}$, and all $T\in\mathcal{T}_h$,

$$\|v_i - I_{T^i}^{k+1}(v_i)\|_{T^i} + h_T^{\frac{1}{2}}\|v_i - I_{T^i}^{k+1}(v_i)\|_{(\partial T)^i} + h_T\|\nabla(v_i - I_{T^i}^{k+1}(v_i))\|_{T^i} \lesssim h_T^{1+\nu}|E_i(v_i)|_{H^{1+\nu}(T^\dagger)}, \tag{31}$$

$$h_T^{\frac{1}{2}}\|[\![v - I_T^{k+1}(v)]\!]_\Gamma\|_{T^\Gamma} \lesssim h_T^{1+\nu}\sum_{j\in\{1,2\}}|E_j(v_j)|_{H^{1+\nu}(T^\dagger)}. \tag{32}$$

The global operator $\hat{I}_h^k$ is built locally by using the operators $\hat{I}_T^k$ defined in (30), and the cell component of $\hat{I}_h^k$ is denoted $I_{\mathcal{T}}^{k+1}$ with its restrictions to each subdomain denoted $I_{\mathcal{T}_i}^{k+1}$, $i\in\{1,2\}$.

Let $v\in H^1(\Omega)$ be such that $v_i \in H^{1+\nu}(\Omega_i)$, $i\in\{1,2\}$, and $B(v) := -\nabla\cdot(\frac{1}{\rho}\nabla v) \in L^2(\Omega)$. The consistency of the discrete bilinear form b_h is measured by the linear form $\delta_h(v;\cdot)\in(\hat{V}_{h0})'$ such that

$$\delta_h(v;\hat{q}_h) := (B(v), q_{\mathcal{T}})_\Omega - b_h(\hat{I}_h^k(v),\hat{q}_h), \qquad \forall \hat{q}_h\in\hat{V}_{h0}. \tag{33}$$

Then it is shown in [6, Lem. 3.9] that

$$\|\delta_h(v;\cdot)\|_{(\hat V_{h0})'} := \sup_{\hat q_h\in\hat V_{h0}\setminus\{0\}} \frac{|\delta_h(v;\hat q_h)|}{\|\hat q_h\|_{\hat V_{h0}}} \lesssim |v|_{*,h}, \tag{34}$$

with

$$\begin{aligned}|v|_{*,h}^2 := \sum_{T\in\mathcal T_h}\sum_{i\in\{1,2\}} \Big\{\rho_i^{-1}\big(\|\boldsymbol\gamma(v)\|_{T^i}^2 + h_T\|\boldsymbol\gamma(v)\|_{(\partial T)^i}^2\big)\Big\} + \rho_1^{-1}h_T\|\boldsymbol\gamma(v)\|_{T^\Gamma}^2 \\ + \sum_{T\in\mathcal T_h}\sum_{i\in\{1,2\}} (\rho_i h_T)^{-1}\|\eta(v)\|_{(\partial T)^i}^2 + (\rho_1 h_T)^{-1}\|[\![\eta(v)]\!]_\Gamma\|_{T^\Gamma}^2,\end{aligned} \tag{35}$$

and $\boldsymbol\gamma(v) := \nabla v - \boldsymbol G_{\mathcal T}(\hat I_h^k(v))$ and $\eta(v)_{|\Omega_i} := v_i - I_{\mathcal T^i}^{k+1}(v)$, $i\in\{1,2\}$.

6.2 H^1-error estimate

We define the discrete error such that, for all $t\in\overline J$,

$$\hat e_h(t) := \hat p_h(t) - \hat I_h^k(p(t)). \tag{36}$$

For a function $\hat v_h\in C^0(\overline J;\hat V_{h0})$, we set $\|\hat v_h\|_{C^0(0,t;\hat V_{h0})} := \sup_{s\in[0,t]}\|\hat v_h(s)\|_{\hat V_{h0}}$ for all $t\in J$. We also define $\Omega^\Gamma := \bigcup_{T\in\mathcal T_h^\Gamma} T$, $\rho_\flat := \min(\rho_1,\rho_2)$, $\rho_\sharp := \max(\rho_1,\rho_2)$, $\kappa_\flat := \min(\kappa_1,\kappa_2)$, and $\chi := (\kappa_\flat/\rho_\sharp)^{\frac12}$.

Theorem 6.1 (H^1-error estimate)**.** *Let p solve* (1) *and let $\hat p_h$ solve* (17) *with the slightly modified initial conditions $p_{\mathcal T}(0)_{|\Omega_i} = I_{\mathcal T^i}^{k+1}(p_{0|\Omega_i})$ and $\partial_t p_{\mathcal T}(0)_{|\Omega_i} = \Pi_{\mathcal T^i}^{k+1}(v_{0|\Omega_i})$, $i\in\{1,2\}$. Assume that $p_{|\Omega_i}\in C^3(\overline J;H^{1+\nu}(\Omega_i))$, $i\in\{1,2\}$, with $\nu\in(\frac12,k+1]$. The following holds for all $t\in J$,*

$$\begin{aligned}\|\partial_t p_{\mathcal T} - I_{\mathcal T}^{k+1}(\partial_t p)\|_{C^0(0,t;L^2(\frac1\kappa;\Omega))} + \|\hat p_h - \hat I_h(p)\|_{C^0(0,t;\hat V_{h0})} \\ \lesssim \Big(|p|_{C^0(0,t;*,h)} + |\partial_t p|_{L^1(0,t;*,h)}\Big),\end{aligned} \tag{37}$$

where we have set

$$|p|_{C^0(0,t;*,h)} := \sup_{s\in[0,t]}\big(|p(s)|_{*,h} + \chi^{-1}\ell_\Omega\|\partial_{tt}p(s) - I_{\mathcal T}^{k+1}(\partial_{tt}p(s))\|_{\frac1\kappa;\Omega^\Gamma}\big), \tag{38}$$

$$|\partial_t p|_{L^1(0,t;*,h)} := \int_0^t \big(|\partial_t p(s)|_{*,h} + \chi^{-1}\ell_\Omega\|\partial_{ttt}p(s) - I_{\mathcal T}^{k+1}(\partial_{ttt}p(s))\|_{\frac1\kappa;\Omega^\Gamma}\big)ds, \tag{39}$$

and $|\cdot|_{*,h}$ is defined in (35)*. Moreover, we have*

$$\|\partial_t p_{\mathcal T} - \partial_t p\|_{C^0(0,t;L^2(\frac1\kappa;\Omega))} + \|\boldsymbol G_{\mathcal T}(\hat p_h) - \nabla p\|_{C^0(0,t;\boldsymbol L^2(\frac1\rho;\Omega))} \lesssim h^\nu\Phi(t,p), \tag{40}$$

with $\Phi(t,p) := \rho_\flat^{-\frac12}\big(|p|_{L^\infty(0,t;H^{1+\nu}(\Omega))} + |\partial_t p|_{L^1(0,t;H^{1+\nu}(\Omega))}\big) + \kappa_\flat^{-\frac12}\chi^{-1}\ell_\Omega h\big(|\partial_{tt}p|_{L^\infty(0,t;H^{1+\nu}(\Omega))} + |\partial_{ttt}p|_{L^1(0,t;H^{1+\nu}(\Omega))}\big)$.

Proof. Step 1: Error equation. We observe that for all $\hat q_h\in\hat V_{h0}$ and all $t\in J$,

$$\begin{aligned}(\partial_{tt}e_{\mathcal T}(t),q_{\mathcal T})_{\frac1\kappa;\Omega} + b_h(\hat e_h(t),\hat q_h) &= (f(t),q_{\mathcal T})_\Omega - (\partial_{tt}I_{\mathcal T}^{k+1}(p(t)),q_{\mathcal T})_{\frac1\kappa;\Omega} - b_h(I_h^k(p(t)),\hat q_h)\\ &= (\partial_{tt}p(t) - I_{\mathcal T}^{k+1}(\partial_{tt}p(t)),q_{\mathcal T})_{\frac1\kappa;\Omega^\Gamma} + \delta_h(p(t);\hat q_h) =: \theta_h(t;\hat q_h),\end{aligned}$$

where we used that $(\partial_{tt}p(t) - I_{\mathcal{T}}^{k+1}(\partial_{tt}p(t)), q_{\mathcal{T}})_{\frac{1}{\kappa};\Omega\setminus\Omega^\Gamma} = 0$ and where the linear form $\delta_h(p(t);\cdot)$ is defined in (33) and bounded in (34). Invoking the Cauchy–Schwarz inequality and Lemma 6.2 (see below) gives

$$\|\theta_h(t;\cdot)\|_{(\hat{V}_{h0})'} \lesssim |p(t)|_{*,h} + \chi^{-1}\ell_\Omega\|\partial_{tt}p(t) - I_{\mathcal{T}}^{k+1}(\partial_{tt}p(t))\|_{\frac{1}{\kappa};\Omega^\Gamma}. \tag{41}$$

Step 2: Stability argument. We test the error equation with $\hat{q}_h = \partial_t\hat{e}_h(t)$ for all $t \in J$. Owing to the symmetry of b_h and integrating by parts in time on the right-hand side, we infer that

$$\frac{d}{dt}\Big\{\frac{1}{2}\|\partial_t e_{\mathcal{T}}(t)\|_{\frac{1}{\kappa};\Omega}^2 + \frac{1}{2}b_h(\hat{e}_h(t),\hat{e}_h(t))\Big\} = \frac{d}{dt}\theta_h(t;\hat{e}_h(t)) - \dot{\theta}(t;\hat{e}_h(t)),$$

where we have set $\dot{\theta}(t;\cdot) := \delta_h(\partial_t p(t);\cdot) + (\partial_{ttt}p(t) - I_{\mathcal{T}}^{k+1}(\partial_{ttt}p(t)),\cdot)_{\frac{1}{\kappa};\Omega^\Gamma}$, so that

$$\|\dot{\theta}_h(t;\cdot)\|_{(\hat{V}_{h0})'} \lesssim |\partial_t p(t)|_{*,h} + \chi^{-1}\ell_\Omega\|\partial_{ttt}p(t) - I_{\mathcal{T}}^{k+1}(\partial_{ttt}p(t))\|_{\frac{1}{\kappa};\Omega^\Gamma}. \tag{42}$$

Integrating in time from 0 to t, observing that $\partial_t e_{\mathcal{T}}(0) = 0$ owing to the initial conditions satisfied by $\hat{p}_h$, and using the coercivity property (28) gives

$$\frac{1}{2}\|\partial_t e_{\mathcal{T}}(t)\|_{\frac{1}{\kappa};\Omega}^2 + \frac{1}{2}\alpha\|\hat{e}_h(t)\|_{\hat{V}_{h0}}^2 \le \theta_h(t;\hat{e}_h(t)) - \theta_h(0;\hat{e}_h(0)) - \int_0^t \dot{\theta}_h(s;\hat{e}_h(s))ds + C\|\hat{e}_h(0)\|_{\hat{V}_{h0}}^2,$$

where the last term results from the boundedness of the discrete bilinear form b_h on $\hat{V}_{h0}\times\hat{V}_{h0}$. Reasoning as in the proof of [9, Thm. 3.1] leads to

$$\frac{1}{2}\|\partial_t e_{\mathcal{T}}\|_{C^0(0,t;L^2(\frac{1}{\kappa};\Omega))}^2 + \frac{1}{8}\alpha\|\hat{e}_h\|_{C^0(0,t;\hat{V}_{h0})}^2 \le C\big(|\theta_h|_{C^0(0,t;(\hat{V}_{h0})')}^2 + |\dot{\theta}_h|_{L^1(0,t;(\hat{V}_{h0})')}^2 + \|\hat{e}_h(0)\|_{\hat{V}_{h0}}^2\big),$$

with $|\theta_h|_{C^0(0,t;(\hat{V}_{h0})')} := \sup_{s\in[0,t]}\|\theta_h(s;\cdot)\|_{(\hat{V}_{h0})'}$ and $|\dot{\theta}_h|_{L^1(0,t;(\hat{V}_{h0})')} := \int_0^t\|\dot{\theta}_h(s;\cdot)\|_{(\hat{V}_{h0})'}ds$. Still reasoning as in this proof (where one uses $e_{\mathcal{T}}(0) = 0$) shows that $\|\hat{e}_h(0)\|_{\hat{V}_{h0}} \lesssim |p_0|_{*,h}$. Combining these bounds with the estimates (41)-(42) proves (37).

Step 3: Convergence rates. The estimate (40) follows from (37) and the triangle inequality, after invoking the approximation properties (31)-(32) and those of the gradient reconstruction from [6, Lem. 3.8]. Notice that the decay rates are optimal if $\nu = k+1$. □

Lemma 6.2 (Poincaré inequality)**.** *We have* $\|q_{\mathcal{T}}\|_\Omega \lesssim \rho_\sharp^{\frac{1}{2}}\ell_\Omega\|\hat{q}_h\|_{\hat{V}_{h0}}$ *for all* $\hat{q}_h \in \hat{V}_{h0}$.

Proof. Let $\hat{q}_h \in \hat{V}_{h0}$. There is $\boldsymbol{v} \in \boldsymbol{H}^1(\Omega)$ such that $\nabla\cdot\boldsymbol{v} = q_{\mathcal{T}}$ and $\|\boldsymbol{v}\|_{\boldsymbol{H}^1(\Omega)} := \big(\|\boldsymbol{v}\|_\Omega^2 + \ell_\Omega^2\|\nabla\boldsymbol{v}\|_\Omega^2\big)^{\frac{1}{2}} \lesssim \ell_\Omega\|q_{\mathcal{T}}\|_\Omega$. Integrating by parts cellwise and re-arranging the terms shows that

$$\begin{aligned}\|q_{\mathcal{T}}\|_\Omega^2 = (q_{\mathcal{T}},\nabla\cdot\boldsymbol{v})_\Omega = \sum_{T\in\mathcal{T}_h}\sum_{i\in\{1,2\}}\big\{-(\nabla q_{T^i},\boldsymbol{v})_{T^i} + (q_{T^i} - q_{(\partial T)^i},\boldsymbol{v}\cdot\boldsymbol{n}_T)_{(\partial T)^i}\big\}\\ + \sum_{T\in\mathcal{T}_h}(\llbracket q_T\rrbracket_\Gamma,\boldsymbol{v}\cdot\boldsymbol{n}_\Gamma)_{T^\Gamma} + \sum_{T\in\mathcal{T}_h}(q_T - q_{\partial T},\boldsymbol{v}\cdot\boldsymbol{n})_{\partial T\cap\Omega},\end{aligned}$$

where we used that $\boldsymbol{v}$ is single-valued at all the mesh interfaces and that q_F vanishes at all the mesh boundary faces. Recalling the definition (27) of the norm $\|\cdot\|_{\hat{V}_{h0}}$, invoking the Cauchy–Schwarz inequality followed by the multiplicative trace inequality (6) (applied componentwise to $\boldsymbol{v}$) gives

$$\|q_{\mathcal{T}}\|_\Omega^2 \lesssim \rho_\sharp^{\frac{1}{2}}\|\hat{q}_h\|_{\hat{V}_{h0}}\Big(\sum_{T\in\mathcal{T}_h}\|\boldsymbol{v}\|_T^2 + h_T^2\|\nabla\boldsymbol{v}\|_T^2\Big)^{\frac{1}{2}},$$

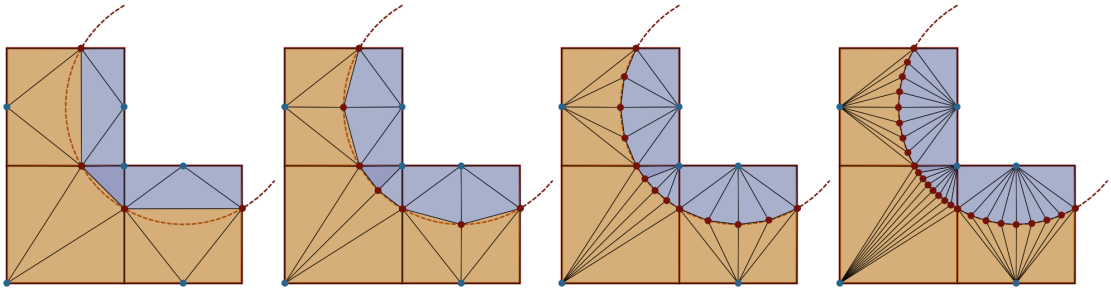

Figure 2: Geometric discretization of the interface and the sub-cells in cut cells. The number of points discretizing the interface is $2^{n_{\mathrm{int}}}+1$ with $n_{\mathrm{int}} \in \{0,1,2,3\}$ (left to right).

where we used Young's inequality to infer that $h_T^{\frac{1}{2}}\|\boldsymbol{v}\|_{\partial(T^i)} \lesssim \|\boldsymbol{v}\|_{T^i} + h_T\|\nabla\boldsymbol{v}\|_{T^i}$ for all $T \in \mathcal{T}_h$ and all $i \in \{1,2\}$. We conclude by observing that $h_T \leq \ell_\Omega$. □

Remark 6.3 (Theorem 6.1)**.** *The difference in the initial condition between* (18) *and Theorem 6.1 only concerns the cut cells $T \in \mathcal{T}_h^\Gamma$ (where the L^2-orthogonal projection uses T and $T^\dagger$ respectively). This choice is a consequence of the use of the error decomposition* (36) *which implies that $e_{\mathcal{T}}(t) = p_{\mathcal{T}}(t) - I_{\mathcal{T}}^{k+1}(p(t))$ which possibly differs from $p_{\mathcal{T}}(t) - \Pi_{\mathcal{T}}^{k+1}(p(t))$ in the cut cells, and in turn, this error decomposition is motivated by the approximation properties* (31)-(32)*. Using $I_{\mathcal{T}}^{k+1}$ in lieu of $\Pi_{\mathcal{T}}^{k+1}$ is also at the origin of the need to invoke the Poincaré inequality from Lemma 6.2 (leading to the velocity factor χ) and the assumption on the third-order time derivative of p (instead of the second-order only). Notice though that the perturbation induced on the factor $\Phi(t,p)$ in* (40) *is of higher order. We believe that these are artifacts of the theoretical analysis, but leave further exploration of these aspects to future work.*

7 Numerical results

In this section, we discuss our numerical results. For the second-order formulation in time (see Section 4), the time discretization is based on the implicit, second-order accurate Newmark scheme with parameters $(\beta,\gamma) = (\frac{1}{4},\frac{1}{2})$. For the first-order formulation in time (see Section 4), the time discretization is based on Runge–Kutta (RK) schemes up to fourth-order accuracy. We consider both singly-diagonally implicit schemes with s stages and order $(s+1)$ with $s \in \{1,2,3\}$ (in short, SDIRK$(s, s+1)$) and explicit schemes with s stages and order s with $s \in \{2,3,4\}$ (in short, ERK(s)). The Butcher tableaux of the RK schemes and their algebraic realization are documented in [8]. Notice that the Newmark scheme is always applied to the second-order formulation in time of the wave equation, whereas the RK schemes are applied to the first-order formulation.

7.1 Implementation

The implementation of fitted HHO methods is discussed in [12]. Here, we focus on implementation aspects related to the unfitted setting.

First, some preprocessing operations are performed on the given Cartesian mesh (background mesh): tagging each geometric entity with an identifier to state whether the object is in Ω_1 or Ω_2; searching for those cells and interfaces that are cut by the interface Γ; identifying the cells with a poor cut and performing a local cell-agglomeration procedure. The agglomeration algorithm is

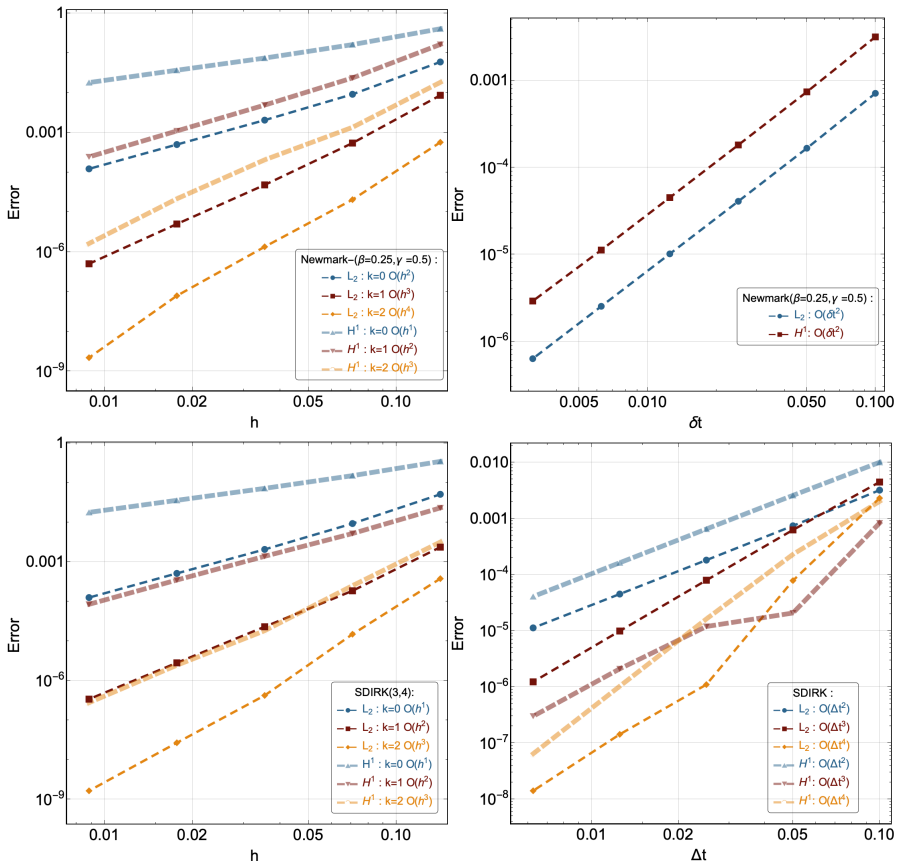

Figure 3: Convergence in space for the analytical solution (44) (left panel), and convergence in time for the analytical solution (45) (right panel). Top row: Newmark scheme; bottom row: SDIRK$(s, s+1)$ scheme with $s = 3$ in the bottom left panel to study the convergence in time and $s \in \{1, 2, 3\}$ in the bottom right panel to study the convergence in time.

detailed in [6, Sec. 5.1] and uses a threshold parameter θ_{agg}. The cell is flagged as being poorly cut if the ratio between the area of each sub-cell and the area of the cell falls below the threshold. Unless stated otherwise, we set $\theta_{\text{agg}} := 0.3$ in our numerical experiments.

To perform numerical integration in the cut cells and along the interface, a set of points is first constructed to discretize the interface as a piecewise affine curve. This set of points is defined by means of a parameter n_{int} so that there are $2^{n_{\text{int}}} + 1$ points discretizing the interface in each cell. Using these points, a sub-triangulation is created in each sub-cell. Finally, the quadrature points and weights are obtained by gathering all the Dunavant [19] quadrature points and weights for all resulting sub-triangles. Figure 2 shows how the sub-triangulation is constructed when $n_{\text{int}} \in \{0, 1, 2, 3\}$. Unless stated otherwise, we use $n_{\text{int}} := 8$ in our numerical experiments.

7.2 Convergence tests for implicit schemes

In this section, we verify the convergence rates delivered by the implicit schemes (Newmark and SDIRK) on smooth solutions in homogeneous media. We also assess the impact of geometry

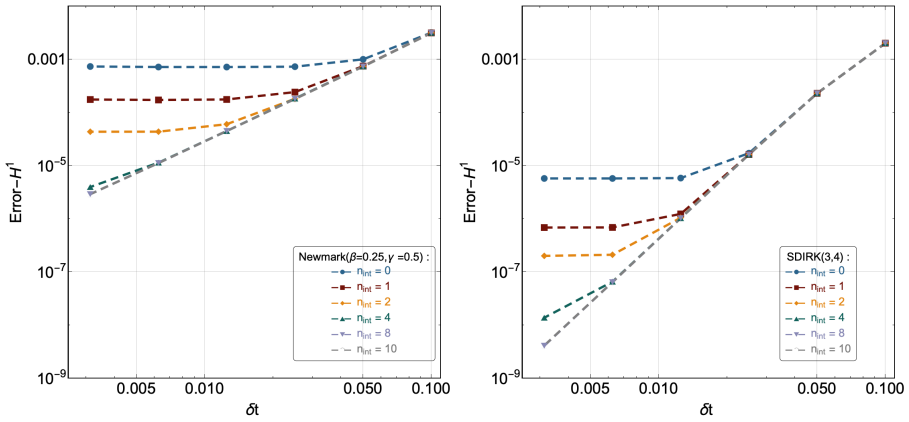

Figure 4: Impact of the choice of the geometry discretization parameter n_{int} in the convergence in time for the analytical solution (45); Newmark scheme (left panel) and SDIRK$(3,4)$ scheme (right panel).

discretization errors. We consider the two-dimensional domain $\Omega := (0,1)^2$, the final time $T_{\text{f}} := 1$, and the material properties are $\rho := \kappa := 1$. The material interface is defined by a circular level set function:

$$\phi_c(x,y) := (x-x_c)^2 + (y-y_c)^2 - r^2, \tag{43}$$

with $r := \frac{1}{3}$ and $x_c = y_c := \frac{1}{2}$. Two smooth solutions are considered:

$$p(t,x,y) = t^2 \sin(\pi x)\sin(\pi y), \tag{44}$$

$$p(t,x,y) = \sin(\sqrt{2}\pi t)x(1-x)y(1-y), \tag{45}$$

where (44) is used to focus on the space discretization error and (45) on the time discretization error. In both cases, the data f and the initial conditions p_0, and v_0 are computed accordingly. We use a sequence of uniformly refined quadrangular meshes of size $h := 0.1 \times 2^{-l}$ with $l \in \{0,1,2,3,4\}$, and the time step size is set to $\Delta t := 0.1 \times 2^{-l}$ with $l \in \{0,1,2,3,4,5\}$. In the following convergence tests, we report the H^1- and L^2-errors at the final time. Figure 3 (upper row) reports the convergence in space for the analytical solution (44) and the convergence in time for the analytical solution (45). The convergence orders in space match the theoretical predictions for smooth solutions, while the convergence in time is of second order as expected. The same conclusions are reached when considering SDIRK schemes (Figure 3, bottom row). Next, we explore the effect of the geometry discretization parameter n_{int} in Figure 4, both for the Newmark and SDIRK schemes. The results confirm that for the values $n_{\text{int}} = \{8, 10\}$, the geometric error is negligible compared to the space and time discretization errors.

7.3 Fitted-unfitted comparison: heterogeneous case with flat interface

The second test case deals with the propagation of an acoustic wave in a two-dimensional heterogeneous domain with a flat interface, so as to allow for the comparison between the fitted and unfitted HHO methods. The domain is $\Omega := (-\frac{3}{2}, \frac{3}{2})^2$, the simulation time is $T_{\text{f}} := 1$, the interface is a line located at $y = 0$, Ω_1 is located below the interface and Ω_2 above. We consider two cases for the material properties: the low-contrast case where $\kappa_1 := 3$, $\kappa_2 := 9$ and $\rho_1 = \rho_2 = 1$ (so that the velocity ratio is $c_2/c_1 = \sqrt{3}$), and the high-contrast case where $\kappa_1 := 3$, $\kappa_2 := 64$

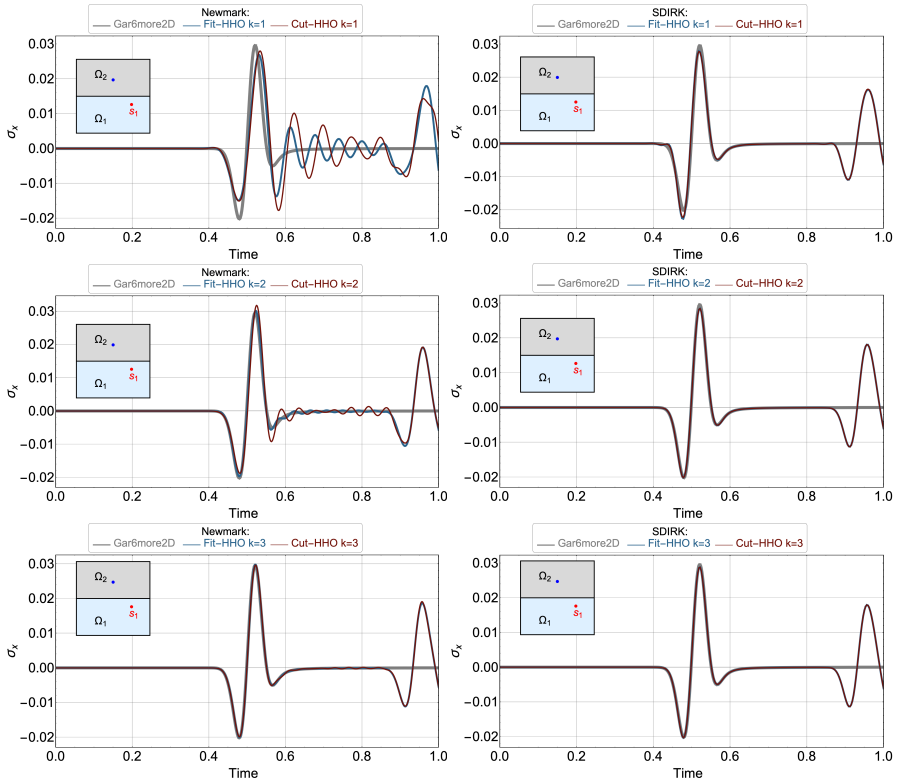

Figure 5: Low-contrast test case. Comparison of the signal σ_x at the sensor S_1 obtained using the semi-analytical solution, the fitted HHO method (Fit-HHO), and the unfitted HHO method (Cut-HHO). Left column: Newmark time-stepping; right column SDIRK$(3,4)$ time-stepping.

and $\rho_1 = \rho_2 = 1$ (so that the velocity ratio is $c_2/c_1 = 8/\sqrt{3}$) The source term is $f \coloneqq 0$, and the initial conditions are $v_0 \coloneqq 0$ and

$$p_0(x,y) \coloneqq \theta \exp\left(-\pi^2 \frac{r^2}{\lambda^2}\right), \tag{46}$$

with $\lambda \coloneqq \frac{c_2}{f}$, $f \coloneqq 10$, $\theta \coloneqq 10\frac{\lambda^2}{2\pi^2}$, $r^2 \coloneqq (x-x_c)^2 + (y-y_c)^2$, $x_c \coloneqq 0$, and $y_c \coloneqq \frac{2}{3}$. The initial condition corresponds to a Ricker wave centered at the point $(x_c, y_c) \in \Omega_2$. The wave first propagates in Ω_2, then is partially transmitted to Ω_1 and later it is also reflected at the boundary of Ω. A semi-analytical solution is available until the wave is reflected at the boundary of Ω, and can be calculated using the `gar6more2d` software.[1] The semi-analytical solution is based on a reformulation of the problem with zero initial conditions and a Dirac source term with a time delay of 0.15 (this value is tuned to match the choice of the parameter θ above).

In our comparisons between the numerical predictions using HHO and the semi-analytical solution, we track the two Cartesian components of $\boldsymbol{\sigma} = \frac{1}{\rho}\nabla p$ at two sensors, one located at the point $S_1 \coloneqq (\frac{3}{4}, -\frac{1}{3})$ in Ω_1 and one located at the point $S_2 \coloneqq (\frac{3}{4}, \frac{1}{3})$ in Ω_2. The comparison with the semi-analytical solution remains valid until the waves reflected at $\partial\Omega$ reach one of the sensors (this happens at about $t_1^* \approx 0.8$ for S_1 and $t_2^* \approx 0.6$ for S_2 in the low-contrast case and at about

[1] see `https://gforge.inria.fr/projects/gar6more2d/`

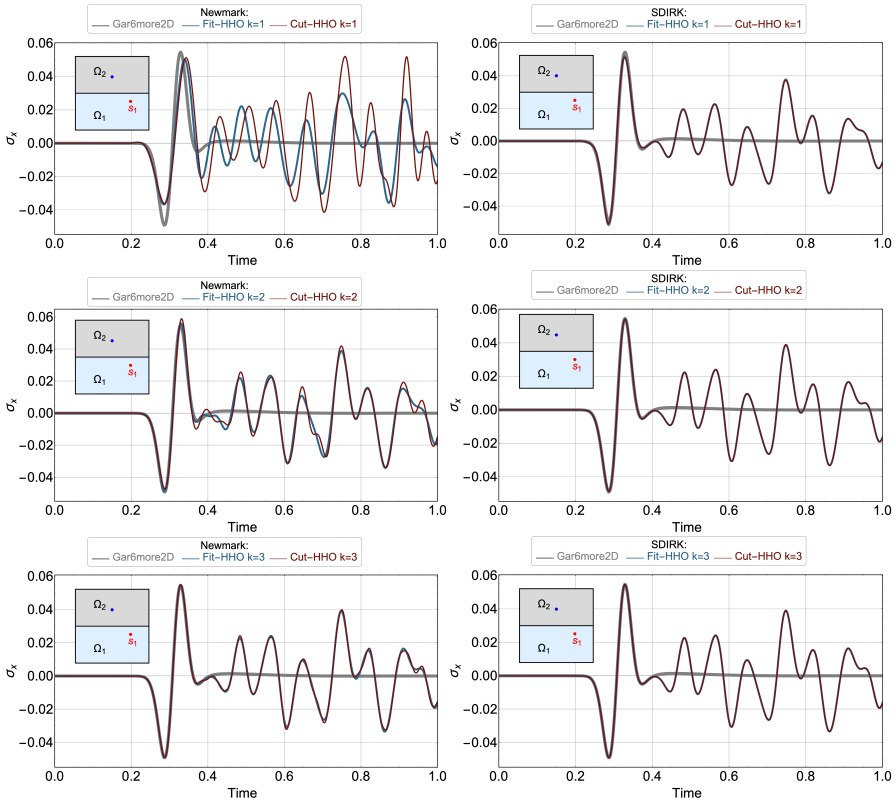

Figure 6: High-contrast test case. Comparison of the signal σ_x at the sensor S_1 obtained using the semi-analytical solution, the fitted HHO method (Fit-HHO), and the unfitted HHO method (Cut-HHO). Left column: Newmark time-stepping; right column SDIRK$(3,4)$ time-stepping.

$t_1^* \approx 0.4$ for S_1 and $t_2^* \approx 0.15$ for S_2 in the high-contrast case). For the numerical predictions, we compare the fitted HHO method from [8] (termed Fit-HHO in the plots) and the unfitted HHO method developed herein (termed Cut-HHO in the plots). The size of the fitted mesh is $h := \frac{1}{32}$, and we consider the polynomial degrees $k \in \{1,2,3\}$. The unfitted mesh is created by agglomerating the 32 cells located just above and just below the interface. Since the interface is flat, we can take $n_{\text{int}} = 0$. For the signal at the sensors, we use the reconstructed gradient in the second-order formulation, and the cell component of $\boldsymbol{\sigma}_{\mathcal{T}}$ in the first-order formulation. The time discretization employs either the Newmark scheme (time steps $\Delta t = 0.1 \times 2^{-7}$ for low contrast and $\Delta t = 0.1 \times 2^{-8}$ for high contrast) or the SDIRK$(3,4)$ scheme (time step $\Delta t = 0.1 \times 2^{-5}$ for low contrast and $\Delta t = 0.1 \times 2^{-6}$ for high contrast).

The results are reported in Figure 5 (low contrast) and in Figure 6 (high contrast) for the x-component at the sensor S_1 (the conclusions are similar for the y-component and for the signals recorded at S_2). We observe in both cases (low and high contrast) that for both time discretization schemes, the choice $k = 1$ for the polynomial order leads to fairly large errors. The situation is improved for $k = 2$, although some oscillations remain for the Newmark scheme, whereas the agreement with the semi-analytical solution is excellent for $k = 3$. We also notice that the results obtained with the fitted HHO method present somewhat less pronounced oscillations than with the unfitted HHO method, although the differences are not very significant and disappear by

Newmark	Fit-HHO			Cut-HHO		
Variable and location	$k=1$	$k=2$	$k=3$	$k=1$	$k=2$	$k=3$
σ_x at S_1	41.43	6.81	3.90	57.07	20.18	4.76
σ_y at S_1	42.85	7.28	4.08	65.02	23.77	5.70
σ_x at S_2	12.14	3.52	3.34	23.77	6.38	3.43
σ_y at S_2	10.76	3.34	3.33	33.18	6.36	3.32

SDIRK$(3,4)$	Fit-HHO			Cut-HHO		
Variable and location	$k=1$	$k=2$	$k=3$	$k=1$	$k=2$	$k=3$
σ_x at S_1	12.91	3.67	2.70	12.32	3.60	2.67
σ_y at S_1	11.89	3.54	2.54	10.09	3.73	2.52
σ_x at S_2	3.12	1.48	1.37	3.14	1.45	1.38
σ_y at S_2	2.29	1.61	1.41	2.42	1.57	1.41

Table 1: Low-contrast case. Maximum relative errors (in %) for the components σ_x and σ_y at the two sensors S_1 and S_2; upper table: Newmark time-stepping; lower table: SDIRK$(3,4)$ time-stepping.

increasing the polynomial degree.

A more quantitative comparison is provided in Table 1 (low contrast) and in Table 2 (high contrast), where we report the maximum relative error (in %) for both components of $\boldsymbol{\sigma}$ over all the discrete time nodes in the time interval $[0, t_i^*]$ for the sensor S_i, $i \in \{1,2\}$. The normalization is computed by using the maximum values in time (in absolute value) obtained for the semi-analytical solution: the resulting values are 2.95×10^{-2} for σ_x at S_1, 7.05×10^{-2} for σ_y at S_1, 7.13×10^{-2} for σ_x at S_2, and 3.17×10^{-2} for σ_y at S_2 in the low-contrast case, and 5.45×10^{-2} for σ_x at S_1, 3.69×10^{-1} for σ_y at S_1, 3.65×10^{-1} for σ_x at S_2, and 1.35×10^{-1} for σ_y at S_2 in the high-contrast case. We observe again the significant improvement gained by increasing the polynomial degree. Moreover, we see that in all cases, the errors incurred with the fitted and unfitted HHO method are comparable, with slightly better results for the fitted version. Observe though that the unfitted mesh is produced by agglomerating two adjacent cells, so that the unfitted HHO methods actually uses twice as large cells around the interface.

7.4 CFL condition for explicit time-stepping

The use of an ERK(s) scheme for time-stepping is subject to a CFL stability condition. The goal of this section is to explore this condition. First, we observe that the condition takes the general form

$$c_\sharp \frac{\Delta t}{h^\gamma} \leq \beta(s)\mu(k), \tag{47}$$

where $c_\sharp$ is the largest velocity in the medium, $\gamma \in \{1,2\}$, $\beta(s) \approx \mathcal{O}(1)$ is a coefficient that depends on the number of stages, and $\mu(k)$ is a coefficient that depends on the mesh geometry and the polynomial degree k (and is expected to scale as $(k+1)^{-1}$). To compute the coefficient $\mu(k)$, we compute numerically on various meshes the largest eigenvalue, say $\lambda_{\max}(h,k)$, of the generalized spectral problem $\mathsf{AX} = \lambda \mathsf{MX}$, where A and M are the stiffness and mass matrices appearing in the algebraic realization (25) of the space semi-discrete HHO formulation with polynomial degree $k \geq 0$. The exponent γ and the coefficient $\mu(k)$ are then determined so that $\mu(k) \approx h^{-\gamma}\lambda_{\max}(h,k)^{-1}$ is h-independent.

Newmark	Fit-HHO			Cut-HHO		
Variable and location	$k=1$	$k=2$	$k=3$	$k=1$	$k=2$	$k=3$
σ_x at S_1	41.31	4.69	1.80	59.43	14.73	2.17
σ_y at S_1	40.75	5.16	1.80	66.25	18.81	2.23
σ_x at S_2	1.29	1.26	1.26	2.08	1.37	1.26
σ_y at S_2	1.26	1.63	1.41	3.01	1.86	1.41

SDIRK$(3,4)$	Fit-HHO			Cut-HHO		
Variable and location	$k=1$	$k=2$	$k=3$	$k=1$	$k=2$	$k=3$
σ_x at S_1	7.20	1.88	0.62	7.47	1.32	0.62
σ_y at S_1	6.95	1.23	0.54	6.39	1.35	0.54
σ_x at S_2	0.23	0.0054	0.00069	0.24	0.0053	0.00057
σ_y at S_2	0.47	0.014	0.0011	0.46	0.015	0.0011

Table 2: High-contrast case. Maximum relative errors (in %) for the components σ_x and σ_y at the two sensors S_1 and S_2; upper table: Newmark time-stepping; lower table: SDIRK$(3,4)$ time-stepping.

k	0	1	2	3
Fit-HHO	0.118	0.0522	0.0338	0.0229
Cut-HHO	0.0765	0.0373	0.0232	0.0159
Ratio	1.5	1.4	1.5	1.4

Table 3: Coefficient $\mu(k)$ for polynomial orders $k \in \{0,1,2,3\}$ and the fitted HHO method (Fit-HHO), the unfitted HHO method (Cut-HHO) together with the ratio of the two values.

In this section, we take $\Omega := (0,1)^2$ and uniform material properties. We consider uniform Cartesian meshes of size $h = 0.1 \times 2^{-l}$ with $l \in \{0,1,2,3,4\}$. First, we consider a flat interface as in the previous section and compare the values obtained for the fitted and unfitted HHO methods. In both cases, our results show (somewhat expectedly) that $\gamma = 1$ if the stabilization weight is $\tilde{\tau}_{\partial T} = \mathcal{O}(1)$ and $\gamma = 2$ if the stabilization weight is $\tilde{\tau}_{\partial T} = \mathcal{O}(h^{-1})$ (see Section 5 for the definition of the weights). This result corroborates that using $\tilde{\tau}_{\partial T} = \mathcal{O}(1)$ is much more effective in the context of ERK(s) schemes than using $\tilde{\tau}_{\partial T} = \mathcal{O}(h^{-1})$, and only the former value is used in the rest of this work. Table 3 reports the value of $\mu(k)$ obtained for the polynomial orders $k \in \{0,1,2,3\}$ for the fitted and unfitted HHO methods. The dependence on the polynomial order is close to $(k+1)^{-1}$ as expected. Moreover, the ratio of the values of $\mu(k)$ for fitted and unfitted HHO is moderate, confirming that the use of the unfitted approach does not really degrade the CFL condition on the time step. Next, we consider a circular interface. The first five panels in Figure 7 (from left to right, top to bottom) highlight the agglomerated cells on the five meshes considered (the agglomeration parameter is set to $\theta_{\text{agg}} = 0.3$). The sixth panel (bottom right) reports the reciprocal of the maximum eigenvalue, $\lambda_{\max}(h,k)^{-1}$, on all the meshes and for the polynomial orders $k \in \{0,1,2,3\}$. We observe that despite the slight irregularity of the agglomeration process as the meshes are refined, the reciprocal of the maximum eigenvalue essentially behaves as h^{-1}. The resulting value of $\mu(k)$ is reported in Table 4 for the agglomeration parameters $\theta_{\text{agg}} \in \{0.1, 0.3, 0.5\}$. As expected, there is a slight increase in $\mu(k)$ as the agglomeration parameter θ_{agg} is decreased since lower values of θ_{agg} favor the presence of cells with worse cuts. However, we see that the impact is moderate since, for instance, the value of $\mu(k)$ for $\theta_{\text{agg}} = 0.1$ is only about 2.5 times worse than the value for $\theta_{\text{agg}} = 0.5$. Interestingly,

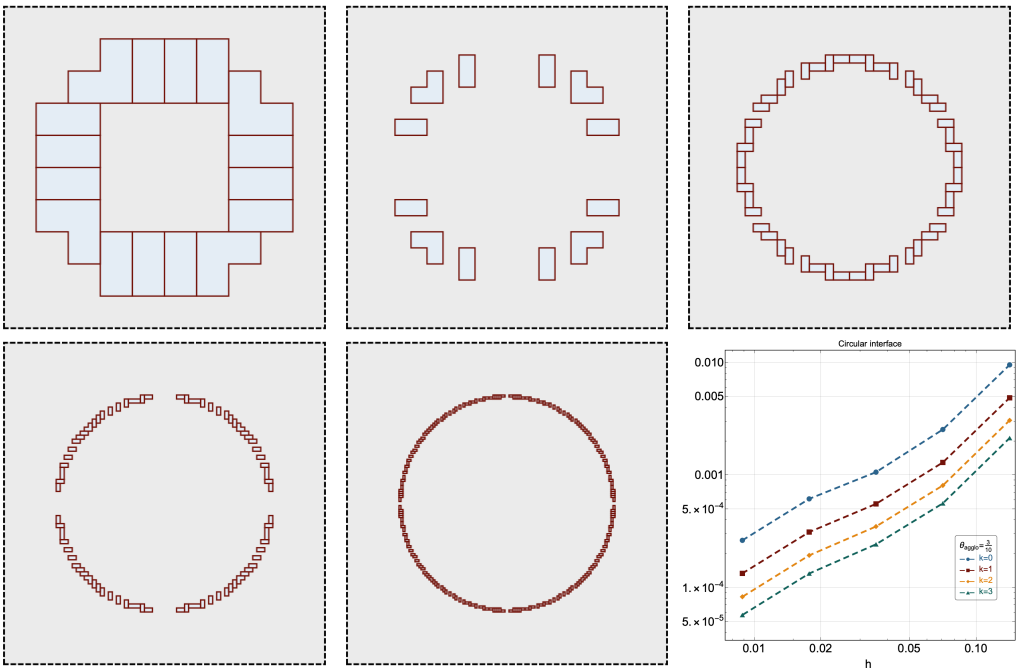

Figure 7: Agglomerated cells for the circular interface on a sequence of successively refined Cartesian meshes of size $h = 0.1 \times 2^{-l}$ with $l \in \{0, 1, 2, 3, 4\}$ (from left to right, top to bottom). Bottom right panel: reciprocal of the maximum eigenvalue, $\lambda_{\max}(h, k)^{-1}$, on all the meshes and for the polynomial orders $k \in \{0, 1, 2, 3\}$.

the value of the ratio is fairly independent of the polynomial degree.

7.5 Comparison of implicit and explicit schemes

The goal of this test case is to compare the computational efficiency of the three time-stepping schemes (Newmark, SDIRK$(3, 4)$, and ERK(4)) on a test case where the interface has a more complex shape than above. Specifically, we employ the following flower-like level set function:

$$\phi_f(x, y) := (x - a)^2 + (y - b)^2 - r^2 - c\cos(n_c\theta), \tag{48}$$

with $a = b := 0$, $r := 1$, $c := \frac{1}{5}$ and $n_c := 8$. For this test case, we consider the same physical settings as in Section 7.3 in the case of low contrast, except for the location of the initial pulse which is now $x_c = y_c := 0$. The sub-domain Ω_2 is the one located inside the flower-like interface, whereas the sub-domain Ω_1 is located outside. Since a semi-analytical solution is no longer available, we compute a reference solution by using SDIRK$(3, 4)$ time-stepping on a Cartesian mesh of size $h := 2^{-6}$, a time step $\Delta t := 0.1 \times 2^{-8}$, and polynomial order $k := 3$. Figure 8 shows the agglomerated cells on the meshes used in the numerical tests (left panel, $h := 2^{-5}$) and to compute the reference solution (right panel, $h := 2^{-6}$). Figure 9 illustrates the propagation of the wave across the flower-like interface and the reflections at the boundary. The selected time values are $t \in \{0.25, 0.5, 1.0\}$.

In order to compare the time-stepping schemes, we set the order of the HHO space semi-discretization to $k := 3$ and we select the value of the time-step for each implicit scheme in

k	0	1	2	3
$\theta_{\text{agg}} = 0.5$	0.042	0.022	0.014	0.0099
$\theta_{\text{agg}} = 0.3$	0.030	0.015	0.0094	0.0065
Ratio	1.4	1.5	1.5	1.5
$\theta_{\text{agg}} = 0.1$	0.017	0.0087	0.0055	0.0039
Ratio	2.5	2.6	2.6	2.5

Table 4: Coefficient $\mu(k)$ for polynomial orders $k \in \{0, 1, 2, 3\}$ and the unfitted HHO method (Cut-HHO) for a circular interface and the agglomeration parameters $\theta_{\text{agg}} \in \{0.1, 0.3, 0.5\}$. The ratios are with respect to the value of $\mu(k)$ obtained with $\theta_{\text{agg}} = 0.5$.

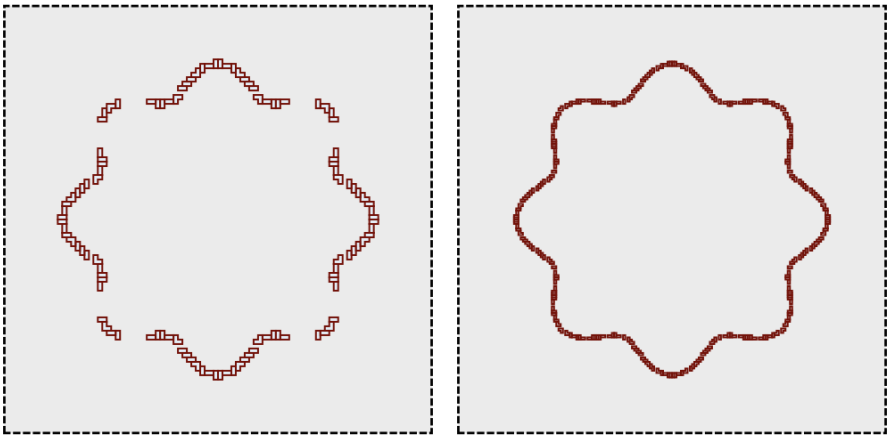

Figure 8: Agglomerated cells for the flower-like interface. Left: mesh used for the numerical comparisons ($h := 2^{-5}$); right: mesh used to compute the reference solution ($h := 2^{-6}$)).

such a way that the accuracy of the signal corresponding to σ_x and σ_y at two sensors is of comparable accuracy. One sensor is located at the point $S_1 := (1.2, 1)$ in Ω_1 and one located at the point $S_2 := (\frac{1}{3}, \frac{2}{3})$ in Ω_2. To refer to the level of time refinement, we write $\Delta t_l := 0.1 \times 2^{-l}$ with $l \in \{4, \ldots, 9\}$ and report the integer l. The mesh-size is $h := 2^{-5}$ for RK schemes and $h := 2^{-6}$ for the Newmark scheme; indeed, the space discretization errors tend to be a bit larger for the Newmark scheme since it handles second-order differential operators in space. Figure 10 reports the signal corresponding to σ_x at the two sensors (similar results are obtained for σ_y) for the Newmark and the SDIRK$(3, 4)$ schemes with polynomial orders $k \in \{1, 2, 3\}$. These results corroborate the benefits of using a high polynomial degree (here, $k = 3$). A more detailed overview of the errors for both signals at both sensors can be found in Table 5 which displays the maximum relative errors (in %) over the time window $t \in [0, 1]$ for the components σ_x and σ_y at the two sensors S_1 and S_2 (the normalization factors are 0.036 for σ_x at S_1, 0.073 for σ_y at S_1, 0.048 for σ_x at S_2, and 0.029 for σ_y at S_2). The conclusion of this study is that we set the time refinement level to $l = 8$ for Newmark and to $l = 6$ for SDIRK$(3, 4)$, leading to relative errors below 2% (for Newmark) or 1% (for SDIRK$(3, 4)$) for the signals at both sensors. Finally, for the ERK(4) scheme, the time refinement level is dictated by the CFL condition and leads to $l = 9$ and to relative errors below 1%.

Table 5 reports some information on the CPU time for the three schemes. We employed the PARDISO sparse linear solver (Intel MKL library) for the direct solver and the Eigen library

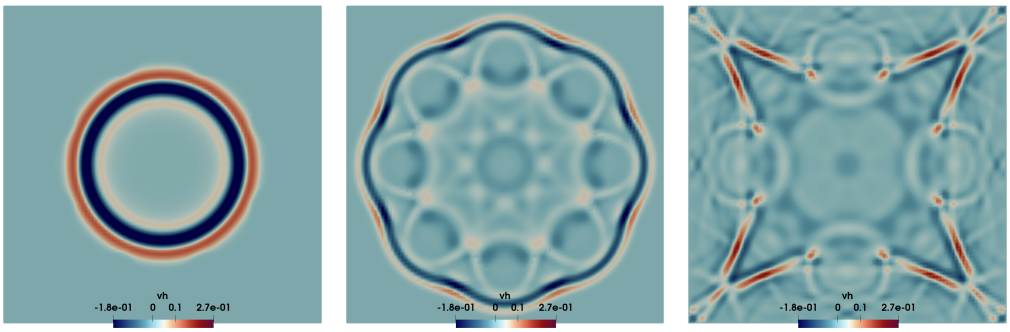

Figure 9: Flower-like test case: reference solution computing using SDIRK$(3,4)$ time-stepping at the times $t \in 0.125, 0.25, 0.5, 1.0$.

Newmark	Polynomial degree			Time ref. level		
Variable and location	$k=1$	$k=2$	$k=3$	$l=6$	$l=7$	$l=8$
σ_x at S_1	15.40	3.954	1.640	10.15	3.817	1.640
σ_y at S_1	16.24	3.977	1.835	11.35	4.272	1.835
σ_x at S_2	2.154	1.506	1.421	7.301	3.115	1.421
σ_y at S_2	2.946	1.469	1.421	7.303	3.116	1.421

SDIRK$(3,4)$	Polynomial degree			Time ref. level		
Variable and location	$k=1$	$k=2$	$k=3$	$l=4$	$l=5$	$l=6$
σ_x at S_1	25.05	2.996	0.3195	20.42	3.333	0.3195
σ_y at S_1	31.72	4.189	0.5562	22.83	4.284	0.5562
σ_x at S_2	8.683	0.4367	0.1281	12.81	1.646	0.1281
σ_y at S_2	7.876	0.2282	0.1201	11.01	1.418	0.1201

Table 5: Flower-like test case. Maximum relative errors (in %) for the components σ_x and σ_y at the two sensors S_1 and S_2. Upper table: Newmark time-stepping; lower table: SDIRK$(3,4)$ time-stepping. For each table, the largest l is considered when varying k, and the largest k when varying l.

implementation of Bi-CGStab for the iterative solver with tolerance 10^{-10}. The reported time values represent the total time per step employed on all the CPUs. The executions were performed on a 8-core CPU (2.7 GHz Quad-Core Intel Core i7) with LPDDR3 memory (16 GB 2133 MHz). All the implementations have been compiled with `clang` including the optimization level `-O3`. The results from Table 6 should be considered as indicative of essential trends, as the current software is not optimized. The first observation is that the efficiency of RK schemes is higher than that of the Newmark scheme. Moreover, if direct solvers are allowed, the lowest overall runtime (time/step multiplied by the number of steps needed to reach final time) is achieved by SDIRK$(3,4)$, whereas if direct solvers are not allowed, the lowest overall runtime is achieved by ERK(4) despite the need to use a smaller time step due to the CFL condition.

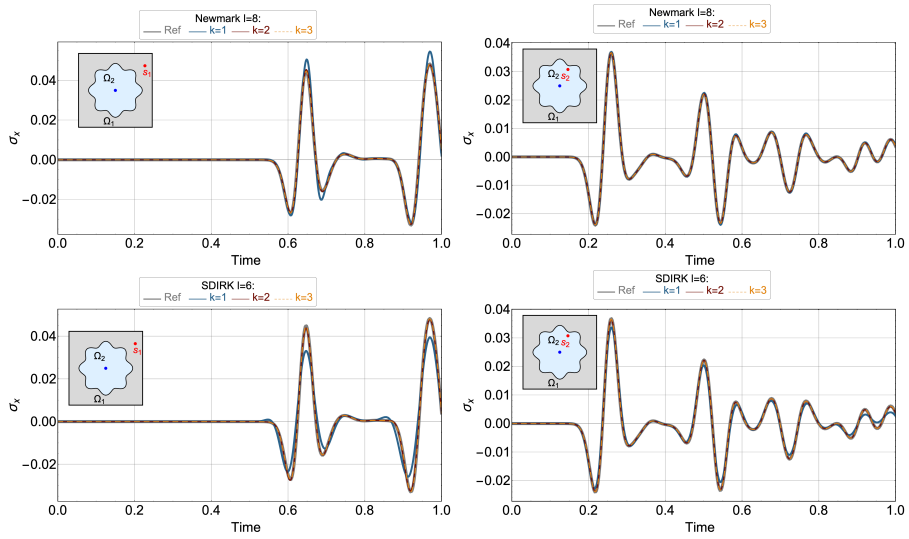

Figure 10: Flower-like test case. Comparison of the signal corresponding to σ_x at the sensors S_1 (left column) and S_2 (right column) for the Newmark scheme (upper row, time refinement level $l = 8$) and the SDIRK$(3, 4)$ scheme (bottom row, time refinement level $l = 6$). The results obtained with polynomial orders $k \in \{1, 2, 3\}$ are compared to the reference solution.

8 Conclusions

We have devised unfitted HHO methods to approximate the acoustic wave equation in heterogeneous media. The unfitted methodology allows the interface to cut the cells in a general fashion, whereas the use of high polynomial orders for the space approximation is beneficial to improve solution accuracy. We have investigated the method theoretically by establishing an H^1-error estimate for the second-order formulation in time, leading to optimal decay rates of the error for smooth solutions. A thorough numerical study has been performed to assess the influence of the discretization of the geometry, the comparable accuracy between fitted and unfitted approaches in the case of a flat interface, and the moderate values of the CFL condition for explicit time-stepping schemes when using the unfitted method with a relatively broad range

scheme	sol.	stab.	time/step	steps	time	err. S_1	err. S_2
ERK(4)	n/a	$\mathcal{O}(1)$	0.194	5120	495.6	0.16	0.02
Newmark	dir.	$\mathcal{O}(h^{-1})$	0.633	2560	1620.0	1.64	1.42
SDIRK$(3, 4)$	dir.	$\mathcal{O}(h^{-1})$	0.717	640	458.9	0.32	0.13
SDIRK$(3, 4)$	iter.	$\mathcal{O}(h^{-1})$	1.018	640	651.7	0.32	0.13

Table 6: Flower-like test case. Comparative efficiency for the Newmark, SDIRK$(3, 4)$, and ERK(4) schemes. The column labeled "sol." reports whether a direct solver or an iterative solver is used, the column labeled "stab." the chocie for the stabilization weight $\tilde{\tau}_{\partial T}$, the column labeled "time/step" the CPU time per time-step [s], the column labeled "steps" the number of time-steps needed to reach the final time, the column labeled "time" the time/step multiplied by the number of steps, and the columns labeled "err" the relative maximum error for σ_x at the two sensors over the time nodes.

of cell-agglomeration parameters. Finally, we have illustrated the capabilities of the proposed methodology in a test case where the interface has a more complex shape and we have performed a comparative study of the efficiency of the various time-stepping schemes. To conclude, we mention that the present study can be extended in a relatively straightforward manner to elastodynamics.

Acknowledgments

The authors would like to thank L. Guillot (CEA/DAM) for insightful discussions and CEA/DAM for partial financial support. EB was partially supported by the EPSRC grants EP/P01576X/1 and EP/P012434/1.

References

[1] M. Abbas, A. Ern, and N. Pignet. Hybrid High-Order methods for finite deformations of hyperelastic materials. *Comput. Mech.*, 62(4):909–928, 2018.

[2] S. Badia, F. Verdugo, and A. F. Martín. The aggregated unfitted finite element method for elliptic problems. *Comput. Methods Appl. Mech. Engrg.*, 336:533–553, 2018.

[3] G. A. Baker. Error estimates for finite element methods for second order hyperbolic equations. *SIAM J. Numer. Anal.*, 13(4):564–576, 1976.

[4] M. Botti, D. A. Di Pietro, and P. Sochala. A Hybrid High-Order method for nonlinear elasticity. *SIAM J. Numer. Anal.*, 55(6):2687–2717, 2017.

[5] E. Burman. Ghost penalty. *C. R. Math. Acad. Sci. Paris*, 348(21-22):1217–1220, 2010.

[6] E. Burman, M. Cicuttin, G. Delay, and A. Ern. An unfitted hybrid high-order method with cell agglomeration for elliptic interface problems. hal-02280426, 2020.

[7] E. Burman, S. Claus, P. Hansbo, M. G. Larson, and A. Massing. CutFEM: discretizing geometry and partial differential equations. *Internat. J. Numer. Methods Engrg.*, 104(7):472–501, 2015.

[8] E. Burman, O. Duran, and A. Ern. Hybrid high-order methods for the acoustic wave equation in the time domain. Available at `https://hal.archives-ouvertes.fr/hal-02922702`, 2020.

[9] E. Burman, O. Duran, A. Ern, and M. Steins. Convergence analysis of HHO methods for the wave equation. hal-02922720, 2020.

[10] E. Burman and A. Ern. An unfitted hybrid high-order method for elliptic interface problems. *SIAM J. Numer. Anal.*, 56(3):1525–1546, 2018.

[11] E. Burman, P. Hansbo, and M. G. Larson. Explicit Time Stepping for the Wave Equation using CutFEM with Discrete Extension. arXiv:2011.05386, 2020.

[12] M. Cicuttin, D. A. Di Pietro, and A. Ern. Implementation of discontinuous skeletal methods on arbitrary-dimensional, polytopal meshes using generic programming. *J. Comput. Appl. Math.*, 344:852–874, 2018.

[13] B. Cockburn, D. A. Di Pietro, and A. Ern. Bridging the hybrid high-order and hybridizable discontinuous Galerkin methods. *ESAIM Math. Model Numer. Anal.*, 50(3):635–650, 2016.

[14] B. Cockburn, Z. Fu, A. Hungria, L. Ji, M. A. Sánchez, and F.-J. Sayas. Stormer-Numerov HDG methods for acoustic waves. *J. Sci. Comput.*, 75(2):597–624, 2018.

[15] B. Cockburn and V. Quenneville-Bélair. Uniform-in-time superconvergence of the HDG methods for the acoustic wave equation. *Math. Comp.*, 83(285):65–85, 2014.

[16] G. C. Cohen. *Higher-Order Numerical Methods for Transient Wave Equations*. Springer Berlin Heidelberg, 2002.

[17] D. A. Di Pietro and A. Ern. A hybrid high-order locking-free method for linear elasticity on general meshes. *Comput. Meth. Appl. Mech. Engrg.*, 283:1–21, 2015.

[18] D. A. Di Pietro, A. Ern, and S. Lemaire. An arbitrary-order and compact-stencil discretization of diffusion on general meshes based on local reconstruction operators. *Comput. Meth. Appl. Math.*, 14(4):461–472, 2014.

[19] D. A. Dunavant. High degree efficient symmetrical Gaussian quadrature rules for the triangle. *Int. J. Numer. Methods Eng.*, 21(6):1129–1148, 1985.

[20] T. Dupont. L^2-estimates for Galerkin methods for second order hyperbolic equations. *SIAM J. Numer. Anal.*, 10:880–889, 1973.

[21] R. S. Falk and G. R. Richter. Explicit finite element methods for symmetric hyperbolic equations. *SIAM J. Numer. Anal.*, 36(3):935–952, 1999.

[22] R. Griesmaier and P. Monk. Discretization of the wave equation using continuous elements in time and a hybridizable discontinuous Galerkin method in space. *J. Sci. Comput.*, 58(2):472–498, 2014.

[23] M. J. Grote, A. Schneebeli, and D. Schötzau. Discontinuous Galerkin finite element method for the wave equation. *SIAM J. Numer. Anal.*, 44(6):2408–2431, 2006.

[24] A. Johansson and M. G. Larson. A high order discontinuous Galerkin Nitsche method for elliptic problems with fictitious boundary. *Numer. Math.*, 123(4):607–628, 2013.

[25] C. Lehrenfeld. *Hybrid Discontinuous Galerkin methods for solving incompressible flow problems*. PhD thesis, Rheinisch-Westfälische Technische Hochschule (RWTH) Aachen, 2010.

[26] C. Lehrenfeld and J. Schöberl. High order exactly divergence-free hybrid discontinuous Galerkin methods for unsteady incompressible flows. *Comput. Methods Appl. Mech. Engrg.*, 307:339–361, 2016.

[27] P. Monk and G. R. Richter. A discontinuous Galerkin method for linear symmetric hyperbolic systems in inhomogeneous media. *J. Sci. Comput.*, 22/23:443–477, 2005.

[28] N. C. Nguyen, J. Peraire, and B. Cockburn. High-order implicit hybridizable discontinuous Galerkin methods for acoustics and elastodynamics. *J. Comput. Phys.*, 230(10):3695–3718, 2011.

[29] M. A. Sánchez, C. Ciuca, N. C. Nguyen, J. Peraire, and B. Cockburn. Symplectic Hamiltonian HDG methods for wave propagation phenomena. *J. Comput. Phys.*, 350:951–973, 2017.

[30] S. Schoeder, S. Sticko, G. Kreiss, and M. Kronbichler. High-order cut discontinuous Galerkin methods with local time stepping for acoustics. *Internat. J. Numer. Methods Engrg.*, 121(13):2979–3003, 2020.

[31] M. Stanglmeier, N. C. Nguyen, J. Peraire, and B. Cockburn. An explicit hybridizable discontinuous Galerkin method for the acoustic wave equation. *Comput. Methods Appl. Mech. Engrg.*, 300:748–769, 2016.

[32] S. Sticko and G. Kreiss. A stabilized Nitsche cut element method for the wave equation. *Comput. Methods Appl. Mech. Engrg.*, 309:364–387, 2016.

[33] S. Sticko and G. Kreiss. Higher order cut finite elements for the wave equation. *J. Sci. Comput.*, 80(3):1867–1887, 2019.

[34] S. Sticko, G. Ludvigsson, and G. Kreiss. High-order cut finite elements for the elastic wave equation. *Adv. Comput. Math.*, 46(3):Paper No. 45, 28, 2020.

[35] S. Terrana, J. P. Vilotte, and L. Guillot. A spectral hybridizable discontinuous Galerkin method for elastic-acoustic wave propagation. *Geophysical Journal International*, 213(1):574–602, 2017.

[36] J. Wang and X. Ye. A weak Galerkin finite element method for second-order elliptic problems. *J. Comput. Appl. Math.*, 241:103–115, 2013.